



# Rotational and High-resolution Infrared Spectrum of HC<sub>3</sub>N: Global Ro-vibrational Analysis and Improved Line Catalog for Astrophysical Observations

Luca Bizzocchi<sup>1</sup> , Filippo Tamassia<sup>2</sup> , Jacob Laas<sup>1</sup> , Barbara M. Giuliano<sup>1</sup>, Claudio Degli Esposti<sup>3</sup>, Luca Dore<sup>3</sup> ,  
 Mattia Melosso<sup>3</sup>, Elisabetta Canè<sup>2</sup>, Andrea Pietropoli Charmet<sup>4</sup>, Holger S. P. Müller<sup>5</sup>, Holger Spahn<sup>5</sup>, Arnaud Belloche<sup>6</sup>,  
 Paola Caselli<sup>1</sup> , Karl M. Menten<sup>6</sup> , and Robin T. Garrod<sup>7</sup>

<sup>1</sup> Center for Astrochemical Studies, Max-Planck-Institut für extraterrestrische Physik, Gießenbachstr. 1,  
 D-85748 Garching bei München, Germany; [bizzocchi@mpe.mpg.de](mailto:bizzocchi@mpe.mpg.de)

<sup>2</sup> Dipartimento di Chimica Industriale “Toso Montanari”, Università di Bologna, viale del Risorgimento 4, I-40136 Bologna, Italy; [filippo.tamassia@unibo.it](mailto:filippo.tamassia@unibo.it)

<sup>3</sup> Dipartimento di Chimica “G. Ciamician”, Università di Bologna, via F. Selmi 2, I-40126 Bologna, Italy

<sup>4</sup> Dipartimento di Scienze Molecolari e Nanosistemi, Università Ca’Foscari Venezia, via Torino 155, I-30172 Mestre Italy

<sup>5</sup> I. Physikalisches Institut, Universität zu Köln, Zùlpicherstraße 77, D-50937 Köln, Germany

<sup>6</sup> Max-Planck-Institut für Radioastronomie, Auf dem Hùgel 69, D-53121 Bonn, Germany

<sup>7</sup> Departments of Chemistry and Astronomy, University of Virginia, Charlottesville, VA 22904, USA

Received 2017 August 3; revised 2017 October 6; accepted 2017 October 9; published 2017 November 22

## Abstract

HC<sub>3</sub>N is a ubiquitous molecule in interstellar environments, from external galaxies to Galactic interstellar clouds, star-forming regions, and planetary atmospheres. Observations of its rotational and vibrational transitions provide important information on the physical and chemical structures of the above environments. We present the most complete global analysis of the spectroscopic data of HC<sub>3</sub>N. We recorded the high-resolution infrared spectrum from 450 to 1350 cm<sup>-1</sup>, a region dominated by the intense  $\nu_5$  and  $\nu_6$  fundamental bands, located at 660 and 500 cm<sup>-1</sup>, respectively, and their associated hot bands. Pure rotational transitions in the ground and vibrationally excited states were recorded in the millimeter and submillimeter regions in order to extend the frequency range so far considered in previous investigations. All of the transitions from the literature and from this work involving energy levels lower than 1000 cm<sup>-1</sup> were fitted together to an effective Hamiltonian. Because of the presence of various anharmonic resonances, the Hamiltonian includes a number of interaction constants, in addition to the conventional rotational and vibrational  $l$ -type resonance terms. The data set contains about 3400 ro-vibrational lines of 13 bands and some 1500 pure rotational lines belonging to 12 vibrational states. More than 120 spectroscopic constants were determined directly from the fit, without any assumption deduced from theoretical calculations or comparisons with similar molecules. An extensive list of highly accurate rest frequencies was produced to assist astronomical searches and data interpretation. These improved data enabled a refined analysis of the ALMA observations toward Sgr B2(N2).

**Key words:** infrared: ISM – ISM: molecules – line: identification – molecular data – radio lines: ISM

**Supporting material:** machine-readable tables

## 1. Introduction

Cyanopolyynes, linear molecules with general formula HC<sub>2n+1</sub>N, are among the most widespread species in astronomical environments. The lightest members of this family are known to be the primary constituents of the interstellar medium (ISM), as they have been identified in a variety of sources along the stellar evolutionary cycle. Their chemistry is linked to that of carbon chains and has been successfully explained by chemical models using specific recipes for the different physical conditions of the various phases of star formation (see Sakai & Yamamoto 2013 for a review). In dark clouds, at early stages, when no protostar has yet ignited, cyanopolyynes are mainly generated by C<sup>+</sup> induced reactions, which proceed until most of the gas-phase carbon is locked in CO and then depleted onto dust grains (e.g., Loison et al. 2014 and references therein). Chains as long as HC<sub>9</sub>N have been firmly identified in these environments, while the detection of HC<sub>11</sub>N in TMC-1 (Bell et al. 1997) was recently disputed by Loomis et al. (2016). At later stages, when the dust temperature rises ( $T \sim 30$ –100 K), the chemistry is regenerated by carbon evaporation under hot core conditions and more chains are produced, mainly by neutral–neutral reactions (Hassel et al. 2008; Sakai et al. 2008).

Cyanoacetylene (HC<sub>3</sub>N), the simplest cyanopolyne, was first discovered toward the Galactic Center by Turner (1971), and it has rapidly arisen as a major astrophysical tracer. Inside the Milky Way, HC<sub>3</sub>N is ubiquitous: it is abundant in starless cores (Suzuki et al. 1992), massive star-forming regions (Li et al. 2012), solar-type protostars (e.g., Jaber Al-Edhari et al. 2017), carbon-rich circumstellar envelopes (Decin et al. 2010), and post-AGB objects (Wyrowski et al. 2003; Pardo et al. 2004). Moreover, its recent detection in protoplanetary disks (Chapillon et al. 2012; Öberg et al. 2014) and comets (Mumma & Charnley 2011) has underlined its potential in an astrobiological context (Öberg et al. 2015), a role that was already suggested many years ago (Sanchez et al. 1966).

HC<sub>3</sub>N has also been detected in external galaxies (e.g., Mauersberger et al. 1990). For example, Costagliola & Aalto (2010) observed vibrationally excited HC<sub>3</sub>N toward NGC 4418 and used it as a probe for the gas physical conditions in a source with intense infrared (IR) fields. The same galaxy was then re-investigated by Costagliola et al. (2015), who highlighted the importance of HC<sub>3</sub>N in luminous infrared galaxies (LIRGs). In recent years, this species has been revealed in other extragalactic sources: IC 342, M66, and NGC 660 (Jiang et al. 2017), NGC 1097 (Martín et al. 2015), and in the nearby

LIRG Mrk 231 by Aalto et al. (2012). Lindberg et al. (2011) published a survey of 13 galaxies in which  $\text{HC}_3\text{N}$  has been detected.

Cyanoacetylene is also an important constituent of the atmosphere of Saturn's major moon, Titan, where it was observed in the millimeter domain by Marten et al. (2002) in the infrared by the CIRS spectrometer on board the *Cassini* spacecraft (Coustenis et al. 2007) and more recently with ALMA (Cordiner et al. 2014). Because of its importance,  $\text{HC}_3\text{N}$  was included in a new astrobiological model of Titan's atmosphere (Willacy et al. 2016).

The outstanding importance of  $\text{HC}_3\text{N}$  for astrophysics and planetary sciences has stimulated vast laboratory activity aimed at studying its spectroscopic properties. The first observation of the pure rotational spectrum of cyanoacetylene dates back to the pioneering times of microwave spectroscopy (Tyler & Sheridan 1963) and the first precise measurements of its ground-state transitions were performed in the centimeter (cm) region by de Zafra (1971) using a molecular beam apparatus. Later, the millimeter (mm) spectrum of  $\text{HC}_3\text{N}$  was recorded by Creswell et al. (1977) and Mallinson & de Zafra (1978), studies that were subsequently extended into the submillimeter (sub-mm) region by Chen et al. (1991) and Yamada et al. (1995). A number of further laboratory studies were devoted to the spectra of its vibrationally excited states (Mallinson & de Zafra 1978; Yamada & Creswell 1986; Mbosei et al. 2000; Thorwirth et al. 2000), and *l*-type transitions between the *l*-doublets of the bending excited states were also recorded (Lafferty 1968; DeLeon & Muentner 1985).

The investigation of the IR laboratory spectrum of  $\text{HC}_3\text{N}$  started in the 1970s and continued in the following decades with a number of low-resolution studies mainly aimed at the measurements of the absolute band intensities (Uyemura & Maeda 1974; Uyemura et al. 1982; Khelifi et al. 1990, 1992). Rotationally resolved measurements were first performed in the  $5\text{ }\mu\text{m}$  spectral region by Yamada et al. (1980) and Yamada & Winnewisser (1981) with an IR diode laser spectrometer. The same authors also carried out a medium-resolution study of the low-energy portion of the mid-IR spectrum (Yamada & Bürger 1986).

Later, Arie et al. (1990) published a detailed high-resolution investigation that covered the  $450\text{--}730\text{ cm}^{-1}$  range. Several vibrational bands were identified, including the  $\nu_5$  and  $\nu_6$  fundamentals, the  $\nu_6 + \nu_7$  combination, plus a number of associated hot bands. This study provided a listing of effective spectroscopic constants for the low-lying vibrational states of  $\text{HC}_3\text{N}$ , which are the most interesting in the context of astrophysics.

As a matter of fact, observations of  $\text{HC}_3\text{N}$  in the ISM very often involve excited vibrational states (e.g., Costagliola et al. 2015; Peng et al. 2017) and, in the context of planetary sciences, a precise model of the observed infrared band profiles must include the associated hot bands (e.g., Jolly et al. 2007). A detailed knowledge of the molecular ro-vibrational pattern is thus a prerequisite for a correct interpretation of the astronomical observations. Because of the numerous perturbations that affect the rotation–vibration spectrum of  $\text{HC}_3\text{N}$ , a global analysis of the laboratory data including both pure rotational and high-resolution IR measurements is necessary in order to derive a compact set of effective spectroscopic parameters without ambiguities and to achieve spectral prediction of high accuracy. To the best of our knowledge,

unlike for the  $\text{HCCC}^{15}\text{N}$  species (Fayt et al. 2004a, 2008), there is no published global analysis for the main isotopologue.

Our purposes are (i) to record new rotational and ro-vibrational spectra, (ii) to perform a global fit of all the literature data with a careful treatment of the resonance effects, and (iii) to provide the best set of spectroscopic constants and a list of highly accurate rest frequencies in the mm and IR spectral regions that are useful for astrophysical applications. The structure of this paper is as follows: in Section 2, we describe the experiments performed in various laboratories; in Section 3, we give a summary of the theory of the vibration–rotation spectra. In Sections 4–5, we describe our ensemble of spectroscopic data and provide some details about the global analysis. In Section 6, we summarize the results, discuss the implications for astrophysics, and report the rest frequency data list. We present our conclusions in Section 7.

## 2. Experiments

A substantial amount of new spectroscopic data of  $\text{HC}_3\text{N}$  was collected in four laboratories located in Bologna, Italy and in Cologne and Munich, Germany. The samples used for the measurements performed in Bologna and in Munich were prepared following the synthetic route described by Miller & Lemmon (1967): propiolamide (Aldrich) was dehydrated with  $\text{P}_4\text{O}_{10}$  at  $225^\circ\text{C}$  under vacuum. The gaseous products were collected in a trap kept at 77 K and then purified by repeated vacuum distillations to remove the volatile side products (mainly  $\text{NH}_3$ ). The remaining white solid, composed of  $\text{HC}_3\text{N}$  plus involatile polymers, was then directly used for spectroscopic measurements and could be stored at  $-25^\circ\text{C}$  over several weeks without significant degradation.

The infrared spectra in the  $450\text{--}1100\text{ cm}^{-1}$  range were recorded in Bologna using a Bomem DA3.002 Fourier-transform spectrometer equipped with a Global source, a KBr beam splitter, and a liquid  $\text{N}_2$ -cooled HgCdTe detector. Path lengths of 0.16, 4, and 5 m were employed. Sample pressures ranging between 16 and 533 Pa were used to record the spectra. The resolution was generally  $0.004\text{ cm}^{-1}$ , except for the very weak  $\nu_4$  band, which was recorded at a lower resolution of  $0.014\text{ cm}^{-1}$ . Several hundreds of scans were co-added in order to improve the signal-to-noise ratio (S/N) of the spectra. The absolute calibration of the wavenumber axis was attained by referencing ro-vibrational transitions of  $\text{H}_2\text{O}$  (Toth 1991) and  $\text{CO}_2$  (Horneman 2007). The accuracy of most line position measurements was estimated to be  $5 \times 10^{-4}\text{ cm}^{-1}$ .

New mm-wave spectra in selected frequency intervals between 80 and 400 GHz were observed in Bologna using a frequency-modulation (FM) mm-wave spectrometer whose details are reported elsewhere (see, e.g., Bizzocchi et al. 2016). The Gunn oscillators, used as the primary radiation sources, were frequency-modulated at 6 kHz and second-harmonic ( $2f$ ) detection was employed. Further measurements of the sub-mm-wave spectrum of  $\text{HC}_3\text{N}$  in the 200–690 GHz frequency range were carried out at the Center for Astrochemical Studies (MPE Garching). The complete description of this experimental apparatus is given in Bizzocchi et al. (2017); here, the radiation source is a Virginia Diode multiplier chain driven by a cm-wave synthesizer. FM at 15 KHz and  $2f$  detection was used. In both laboratories, the spectra were recorded at room temperature, using static samples at a pressure of  $\sim 0.5$  Pa. The transition frequencies were recovered from a

line-shape analysis of the spectral profile (Dore 2003), and their accuracy, estimated by repeated measurements, was in the 5–30 kHz range, depending on the attained S/N.

The measurements performed in Cologne were carried out with leftover samples from previous studies (Yamada et al. 1995; Thorwirth et al. 2000). Eight transitions pertaining to  $v_5 = v_7 = 1$  ( $J = 39, 41$ ) remained unpublished by Thorwirth et al. (2000). Ground-state transition frequencies were recorded in the 3 mm region ( $J = 8$  to 12) to assess the best accuracy attainable for Doppler-limited measurements of this molecule. A 4 m long single-pass Pyrex glass cell equipped with PTFA windows was used for static measurements at room temperature and at pressures of 0.1 Pa or lower. A backward-wave oscillator (BWO) based 3 mm synthesizer AM-MSP 2 was employed as source and a liquid He-cooled InSb bolometer as detector. Calibration measurements were made on the  $J = 1 - 0$ , CO line whose frequency is known to an accuracy of 0.5 kHz from sub-Doppler measurements (Winnewisser et al. 1997). After adjustment, this line was measured in the Doppler regime with a precision of  $\sim 2$  kHz.

Further measurements were made using the Cologne Terahertz Spectrometer (CTS; see Winnewisser 1995 for a detailed description of the apparatus). Room-temperature static samples at pressures of 0.1 Pa were employed for stronger lines and up to about 1 Pa for the weaker ones. A few lines were recorded around 610, 800, and 900 GHz. These measurements were aimed at improving the data set for some vibrationally excited states not investigated by Thorwirth et al. (2000) and at achieving a general spectral coverage extending beyond  $J = 100$ . Measurement accuracies for isolated lines with very symmetric shapes ranged from 5 kHz to mostly 10–20 kHz. Weaker or less symmetric lines or lines close to others were given larger uncertainties. The measurements and the accuracies are similar to those of DC<sub>3</sub>N, described in Spahn et al. (2008).

### 3. Theory

#### 3.1. Notation for States and Wave Functions

The analysis presented in this paper involves, as far as the ro-vibrational data are concerned, transitions arising from the ground state and four vibrationally excited states located below 1100 cm<sup>-1</sup>:  $v_7$  (C–CN bend),  $v_6$  (CCC bend),  $v_5$  (H–CC bend), and  $v_4$  (C–C stretch). All of the other vibrational modes are not considered, thus a given vibrational state can be labelled using the notation  $(v_4, v_5^{l_5}, v_6^{l_6}, v_7^{l_7})_{e/f}$ , where  $l_i$  quantum numbers label the vibrational angular momentum associated with each  $v_i$  bending mode. The  $e/f$  subscripts indicate the parity of the symmetrized wave functions following the usual convention for linear molecules (Brown et al. 1975). When there is no ambiguity, the simplified notation  $(l_5, l_6, l_7)_{e/f}$  will be used in the text to identify the different sublevels of a bending state.

The ro-vibrational wave functions are represented by the ket  $|v_4, v_5^{l_5}, v_6^{l_6}, v_7^{l_7}; J, k\rangle_{e/f}$ . The vibrational part is expressed as a product of one- and two-dimensional harmonic oscillator wave functions, while the rotational part is the symmetric-top wave function where the angular quantum number  $k$  is subjected to the constraint  $k = l_5 + l_6 + l_7$ . Symmetry-adapted basis functions are obtained using the following Wang-type linear

combinations (Yamada et al. 1985):

$$\begin{aligned} & |v_4, v_5^{l_5}, v_6^{l_6}, v_7^{l_7}; J, k\rangle_{e/f} \\ &= \frac{1}{\sqrt{2}} \{ |v_4, v_5^{l_5}, v_6^{l_6}, v_7^{l_7}; J, k\rangle \\ &\pm (-1)^k |v_4, v_5^{-l_5}, v_6^{-l_6}, v_7^{-l_7}; J, -k\rangle \}, \end{aligned} \quad (1a)$$

$$|v_4, 0^0, 0^0, 0^0; J, 0\rangle_e = |v_4, 0^0, 0^0, 0^0; J, 0\rangle. \quad (1b)$$

The upper and lower signs ( $\pm$ ) correspond to the  $e$  and  $f$  wave functions, respectively. For  $\Sigma$  states ( $k = 0$ ), the first non-zero  $l_i$  is chosen to be positive. Note that the omission of the  $e/f$  label indicates unsymmetrized wave functions.

#### 3.2. Ro-vibrational Hamiltonian

The observed transition frequencies are expressed as differences between ro-vibrational energy eigenvalues; these are computed using an effective Hamiltonian adapted for a linear molecule:

$$\tilde{H} = \tilde{H}_{\text{vr}} + \tilde{H}_{l\text{-type}} + \tilde{H}_{\text{res}}, \quad (2)$$

where  $\tilde{H}_{\text{vr}}$  represents the ro-vibrational energy including centrifugal distortion,  $\tilde{H}_{l\text{-type}}$  is the  $l$ -type interaction energy among the  $l$ -sublevels of excited bending states, and  $\tilde{H}_{\text{res}}$  is the contribution due to the ro-vibrational resonances between accidentally quasi-degenerate states.

The Hamiltonian matrix is set up using unsymmetrized ro-vibrational basis functions; it is then factorized and symmetrized using Equation (1). The matrix elements of the effective Hamiltonian are expressed using the formalism first introduced by Yamada et al. (1985) and already employed for analysis of the ro-vibrational spectra of several carbon chains with multiple bending vibrations (see, e.g., Degli Esposti et al. 2005). Here, the following shorthand will be used to simplify the notation:

$$f_0(J, k) = J(J + 1) - k^2, \quad (3a)$$

$$f_{\pm n}(J, k) = \prod_{p=1}^n J(J + 1) - [k \pm (p - 1)](k \pm p). \quad (3b)$$

The  $\tilde{H}_{\text{vr}}$  term of the Hamiltonian is purely diagonal in all  $v$  and  $k$  quantum numbers. It has the form

$$\begin{aligned} \langle l_5, l_6, l_7; k | \tilde{H}_{\text{vr}} | l_5, l_6, l_7; k \rangle &= \sum_t x_{L(t)} l_t^2 \\ &+ \sum_{t \neq 7} x_{L(t7)} l_t l_7 + \sum_t y_{L(t)} l_t^4 \\ &+ \left\{ B_v + \sum_t d_{JL(t)} l_t^2 + \sum_{t \neq 7} d_{JL(t7)} l_t l_7 \right\} f_0(J, k) \\ &- \left\{ D_v + \sum_t h_{JL(t)} l_t^2 + \sum_{t \neq 7} h_{JL(t7)} l_t l_7 \right\} f_0(J, k)^2 \\ &+ \left\{ H_v + \sum_t l_{JL(t)} l_t^2 \right\} f_0(J, k)^3. \end{aligned} \quad (4)$$

The  $\tilde{H}_{l\text{-type}}$  term of the Hamiltonian is also diagonal in  $v$ , but it features contributions that are off-diagonal in the quantum numbers  $l_i$  and with  $\Delta k = 0, \pm 2, \pm 4$ .

The vibrational  $l$ -type doubling terms with  $\Delta k = 0$  have the general formula

$$\begin{aligned} &\langle l_t \pm 2, l_{t'} \mp 2; k | \tilde{H}_{l\text{-type}} | l_t, l_{t'}; k \rangle \\ &= \frac{1}{4} \{ r_{tt'} + r_{tt'} J(J+1) + r_{tt'JJ} J^2(J+1)^2 \} \\ &\times \sqrt{(v_t \mp l_t)(v_t \pm l_t + 2)(v_{t'} \mp l_{t'} + 2)(v_{t'} \pm l_{t'})}. \end{aligned} \quad (5)$$

The rotational  $l$ -type resonance terms with  $\Delta k = \pm 2$  are expressed by

$$\begin{aligned} &\langle l_t \pm 2; k \pm 2 | \tilde{H}_{l\text{-type}} | l_t; k \rangle \\ &= \frac{1}{4} \{ q_t + q_{tJ} J(J+1) + q_{tJJ} J^2(J+1)^2 \} \\ &\times \sqrt{(v_t \mp l_t)(v_t \pm l_t + 2) f_{\pm 2}(J, k)}, \end{aligned} \quad (6)$$

$$\begin{aligned} &\langle l_t \mp 2, l_{t'} \pm 4; k \pm 2 | \tilde{H}_{l\text{-type}} | l_t, l_{t'}; k \rangle \\ &= \frac{1}{8} q_{tt'} \{ (v_t \mp l_t + 2)(v_t \pm l_t)(v_{t'} \mp l_{t'}) \\ &\times (v_{t'} \pm l_{t'} + 2)(v_{t'} \mp l_{t'} - 2)(v_{t'} \pm l_{t'} + 4) \}^{1/2} \sqrt{f_{\pm 2}(J, k)} \end{aligned} \quad (7)$$

The terms relative to  $\Delta k = \pm 4$  are

$$\begin{aligned} &\langle l_t \pm 4; k \pm 4 | \tilde{H}_{l\text{-type}} | l_t; k \rangle = \frac{1}{4} u_{tt} \{ (v_t \mp l_t)(v_t \pm l_t + 2) \\ &\times (v_t \mp l_t - 2)(v_t \pm l_t + 4) \}^{1/2} \sqrt{f_{\pm 4}(J, k)}, \end{aligned} \quad (8)$$

$$\begin{aligned} &\langle l_t \pm 2, l_{t'} \pm 2; k \pm 4 | \tilde{H}_{l\text{-type}} | l_t, l_{t'}; k \rangle \\ &= \frac{1}{4} u_{tt'} \{ (v_{t'} \mp l_{t'})(v_{t'} \pm l_{t'} + 2) \\ &\times (v_t \mp l_t)(v_t \pm l_t + 2) \}^{1/2} \sqrt{f_{\pm 4}(J, k)}. \end{aligned} \quad (9)$$

Following Wagner et al. (1993), the terms of the effective Hamiltonian for the ro-vibrational resonances can be written as

$$\tilde{H}_{\text{res}} = \sum_{m,n} C_{mn} \hat{\mathcal{L}}^m \hat{J}^n, \quad (10)$$

where  $C_{mn}$  is the resonance coefficient,  $m$  is the total degree in the vibrational ladder operators  $\hat{\mathcal{L}}^\pm$ , and  $n$  is the total degree in the rotational angular momentum operators  $\hat{J}$  (Wagner et al. 1993; Okabayashi et al. 1999). Here, we want to discuss briefly the order of magnitude of the terms connecting the interacting states. Given the complexity of the HC<sub>3</sub>N resonance network, order-of-magnitude considerations are very useful to assess which terms matter in a given range of energy and quantum numbers and which can be safely ignored.

The order of magnitude of the terms in the rotation–vibration Hamiltonian is usually expressed as the Born–Oppenheimer expansion parameter,  $\kappa = (m_e/m_n)^{1/4}$ , where  $m_e$  and  $m_n$  are the electronic and nuclear masses, respectively (Oka 1967). For ro-vibrational spectroscopy applications, a suitable estimate is  $\kappa = (B/\omega_{\text{vib}})^{1/2}$ , where  $\omega_{\text{vib}}$  is a typical harmonic vibrational frequency and  $B$  is the rotational constant (Nielsen 1951). For HC<sub>3</sub>N,  $\kappa \simeq 1/56$ , taking  $B \sim 0.15 \text{ cm}^{-1}$  and  $\omega_{\text{vib}} \sim 500 \text{ cm}^{-1}$ . Following Aliev & Watson (1985), the general expression for the order of magnitude of the effective Hamiltonian element,  $\tilde{H}_{mn}$ , can be written as

$$\tilde{H}_{mn} \approx r^m J^n \kappa^{m+2n-2} \omega_{\text{vib}}, \quad (11)$$

where  $r$  is either the vibrational coordinate  $q$  or the vibrational momentum  $p$ , and  $J$  is the rotational quantum number. This

**Table 1**  
Order-of-magnitude Classification of the Resonance Operators

Terms	Order of Magnitude	
	$\kappa^{m+n-2} \omega_{\text{vib}}$ “Exact” Resonance	$\kappa^{2m+2n-5} \omega_{\text{vib}}$ Close Interacting Levels
$\tilde{H}_{30}$	$\kappa \omega_{\text{vib}}$	$\kappa \omega_{\text{vib}}$
$\tilde{H}_{31}, \tilde{H}_{40}$	$\kappa^2 \omega_{\text{vib}}$	$\kappa^3 \omega_{\text{vib}}$
$\tilde{H}_{32}, \tilde{H}_{50}$	$\kappa^3 \omega_{\text{vib}}$	$\kappa^5 \omega_{\text{vib}}$
$\tilde{H}_{33}, \tilde{H}_{42}$	$\kappa^4 \omega_{\text{vib}}$	$\kappa^7 \omega_{\text{vib}}$
$\tilde{H}_{52}, \tilde{H}_{34}$	$\kappa^5 \omega_{\text{vib}}$	$\kappa^9 \omega_{\text{vib}}$
$\tilde{H}_{44}$	$\kappa^6 \omega_{\text{vib}}$	$\kappa^{11} \omega_{\text{vib}}$
$\tilde{H}_{54}$	$\kappa^7 \omega_{\text{vib}}$	$\kappa^{13} \omega_{\text{vib}}$

latter dependence accounts for resonances that involve rotational operators: these terms can be ignored at low or moderate values of  $J$  but may become important as  $J$  increases.

For low vibrational quantum numbers,  $r \simeq 1$ , and if one assumes  $J \simeq \kappa^{-1} \simeq 56$ , the order of magnitude of the  $\tilde{H}_{mn}$  contribution is  $\kappa^{m+n-2} \omega_{\text{vib}}$  for exact resonances. For less close resonances, the contribution to the ro-vibrational energy of the matrix element  $H_{mn}$  can be estimated through the second-order perturbation formula

$$E \simeq \frac{H_{mn}^2}{\Delta} \simeq \kappa^{2m+2n-4} \left( \frac{\omega_{\text{vib}}}{\Delta} \right) \omega_{\text{vib}}. \quad (12)$$

The quantity  $\Delta$  in the denominator of Equation (12) is the energy difference between the two vibrational levels. For interacting states, whose energy difference is  $\Delta \simeq 10 \text{ cm}^{-1}$ , one can assume  $\omega_{\text{vib}}/\Delta \simeq \kappa^{-1}$ . The contribution of  $\tilde{H}_{mn}$  to the ro-vibrational energy is then  $\kappa^{2m+2n-5} \omega_{\text{vib}}$ .

The order-of-magnitude classification of the various Hamiltonian terms is summarized in Table 1, where, in the first column, we listed all of the resonance operators that may be relevant for the analysis of the spectra described in this paper. It is important to notice that the overall rank of the individual terms is preserved in the two cases described. Only the power of  $\kappa$  diverges more rapidly in close-resonance cases. This implies that, once we choose the cutting threshold for the power of  $\kappa$  for the terms to be considered in the analysis, more interactions have to be taken into account in the case of “exact” resonances with respect to the close-resonance situation.

The resonance network present in the energy-level manifold of HC<sub>3</sub>N below  $1000 \text{ cm}^{-1}$  was already described and partially analyzed by Yamada & Creswell (1986). However, given the higher level of detail of our investigation, a number of extra terms were evaluated. As a general guideline, energy contributions of order higher than  $\kappa^5 \omega_{\text{vib}}$  ( $< 0.03 \text{ MHz}$ ) can be safely ignored.

Our analysis indicates that  $\tilde{H}_{30}$ ,  $\tilde{H}_{31}$ , and  $\tilde{H}_{40}$  must be considered, and  $\tilde{H}_{32}$  and  $\tilde{H}_{50}$  can be important for close interacting levels. On the other hand,  $\tilde{H}_{42}$  and  $\tilde{H}_{52}$  might produce only minor effects on very close resonances and their importance can be significantly enhanced for high- $v$ , high- $J$  levels. In Equations (13)–(18), we list all of the resonance terms included in the spectral analysis.

The cubic anharmonic interactions of the  $(v_4, v_5, v_6, v_7)$  state with the  $(v_4 + 1, v_5, v_6 - 2, v_7)$ , and  $(v_4 + 1,$



$v_5 - 1, v_6, v_7 - 1$  states are expressed by

$$\begin{aligned} & \langle v_4, v_5^{l_5}, v_6^{l_6}, v_7^{l_7}; J, k | \tilde{H}_{30} \\ & + \tilde{H}_{32} | v_4 + 1, v_5^{l_5}, (v_6 - 2)^{l_6}, v_7^{l_7}; J, k \rangle \\ & = \sqrt{2} [(v_4 + 1)(v_6 + l_6)(v_6 - l_6)]^{1/2} \\ & \times \{C_{30}^{(466)} + C_{32}^{(466J)} J(J + 1)\}, \end{aligned} \quad (13)$$

$$\begin{aligned} & \langle v_4, v_5^{l_5}, v_6^{l_6}, v_7^{l_7}; J, k | \tilde{H}_{30} \\ & + \tilde{H}_{32} | v_4 + 1, (v_5 - 1)^{l_5 \pm 1}, v_6^{l_6}, (v_7 - 1)^{l_7 \mp 1}; J, k \rangle \\ & = \frac{\sqrt{2}}{2} [(v_4 + 1)(v_5 \mp l_5)(v_7 \pm l_7)]^{1/2} \\ & \times \{C_{30}^{(457)} + C_{32}^{(457J)} J(J + 1)\}. \end{aligned} \quad (14)$$

The quartic anharmonic interaction coupling the  $(v_5, v_7)$  and  $(v_5 + 1, v_7 - 3)$  states is given by

$$\begin{aligned} & \langle v_5^{l_5}, v_7^{l_7}; J, k | \tilde{H}_{40} + \tilde{H}_{42} | (v_5 + 1)^{l_5 \pm 1}, (v_7 - 3)^{l_7 \mp 1}; J, k \rangle \\ & = \frac{1}{4} [(v_5 \pm l_5 + 2)(v_7 \pm l_7)(v_7 \mp l_7)(v_7 \pm l_7 - 2)]^{1/2} \\ & \times \{C_{40}^{(5777)} + C_{42}^{(5777J)} J(J + 1)\}. \end{aligned} \quad (15)$$

The quintic anharmonic resonance between the  $(v_4, v_7)$  and  $(v_4 + 1, v_7 - 4)$  states is

$$\begin{aligned} & \langle v_4, v_7^{l_7}; J, k | \tilde{H}_{50} + \tilde{H}_{52} | (v_4 + 1), (v_7 - 4)^{l_7}; J, k \rangle \\ & = \frac{\sqrt{2}}{2} [(v_4 + 1)(v_7 + l_7 - 2)(v_7 - l_7 - 2) \\ & \times (v_7 + l_7)(v_7 - l_7)]^{1/2} \{C_{50}^{(47777)} + C_{52}^{(47777J)} J(J + 1)\}. \end{aligned} \quad (16)$$

In association with the classic quartic anharmonic resonance, we took into account two further terms generated by the  $\tilde{H}_{42}$  Hamiltonian and that are off-diagonal both in  $v$  and in  $l$ . They are

$$\begin{aligned} & \langle v_5^{l_5}, v_7^{l_7}; J, k | \tilde{H}_{42} | (v_5 + 1)^{l_5 \pm 1}, (v_7 - 3)^{l_7 \pm 1}; J, k \pm 2 \rangle \\ & = \frac{1}{4} [(v_5 \pm l_5 + 2)(v_7 + l_7)(v_7 - l_7)(v_7 \mp l_7 + 2)]^{1/2} \\ & \times C_{42a}^{(5777)} \sqrt{f_{\pm 2}(J, k)}, \end{aligned} \quad (17)$$

$$\begin{aligned} & \langle v_5^{l_5}, v_7^{l_7}; J, k | \tilde{H}_{42} | (v_5 + 1)^{l_5 \pm 1}, (v_7 - 3)^{l_7 \mp 3}; J, k \mp 2 \rangle \\ & = \frac{1}{4} [(v_5 \pm l_5 + 2)(v_7 \pm l_7)(v_7 \pm l_7 - 2)(v_7 \mp l_7 - 4)]^{1/2} \\ & \times C_{42b}^{(5777)} \sqrt{f_{\mp 2}(J, k)}. \end{aligned} \quad (18)$$

Other possible couplings are the quartic anharmonic interaction between the  $(v_5, v_6, v_7)$  and  $(v_5 + 1, v_6 - 2, v_7 + 1)$  states generated by  $\tilde{H}_{40}$ , plus the  $\tilde{H}_{31}$  Coriolis-type resonances that couple the states  $(v_6, v_7)$  and  $(v_6 + 1, v_7 - 2)$ , and  $(v_5, v_6, v_7)$  and  $(v_5 + 1, v_6 - 1, v_7 - 1)$ . These interactions were found to be important in the global fit of the infrared and rotational spectra of the  $\text{HCCC}^{15}\text{N}$  isotopologue (Fayt et al. 2004a, 2008). We tested these terms in the  $\text{HC}_3\text{N}$  analysis, but they produced only minor effects and the corresponding coefficients were poorly determined. Hence, these interactions were not considered in the final fit (see also Sections 5.1 and 6.1).

## 4. Observed Spectra

### 4.1. Infrared Spectrum

The infrared spectra recorded in the laboratory cover the 450–1350  $\text{cm}^{-1}$  interval. However, we decided to study in this work only the ro-vibrational bands corresponding to vibrational levels with energy lower than 1000  $\text{cm}^{-1}$ . This choice allowed us to perform a complete analysis of the low-lying vibrational states involved in anharmonic resonances present in  $\text{HC}_3\text{N}$ . In total, 13 IR bands were recorded and analyzed. Figure 1 shows the bottom part of the vibrational energy diagram of  $\text{HC}_3\text{N}$  up to circa 1300  $\text{cm}^{-1}$ . The plot marks the investigated states and the IR transitions considered in the analysis. The overview of the  $\text{HC}_3\text{N}$  high-resolution vibrational spectrum over the full wavenumber range covered by this study is shown in Figure 2. In the mid-IR region, the  $\text{HC}_3\text{N}$  vibrational spectrum is dominated by the very strong bending fundamentals  $\nu_5$  and  $\nu_6$  located at  $\sim 660 \text{ cm}^{-1}$  and  $\sim 500 \text{ cm}^{-1}$ , respectively. Other weaker combination and overtone bands are visible at higher wavenumbers. The  $\nu_4$  stretching fundamental located at  $\sim 873 \text{ cm}^{-1}$  is very weak ( $I(\nu_5)/I(\nu_4) \sim 1/400$ ; Jolly et al. 2007) and could be observed only with a long integration time (2100 scans) at a pressure of 270 Pa and 4 m optical path length. The spectral resolution was also lowered to 0.014  $\text{cm}^{-1}$ . The strongest  $\nu_5$  and  $\nu_6$  band systems are particularly crowded because of the presence of numerous hot bands that are intense enough to be easily revealed. Many  $Q$ -branches due to these fundamentals and their  $\nu_7$ -associated hot bands are clearly visible in the recorded spectrum near the corresponding band centers as shown in Figures 3 and 4.

Table 2 summarizes the subset of bands that were assigned and analyzed in this study. It comprises all but three bands that have been previously recorded by Arie et al. (1990). The exceptions are the hot bands involving  $2\nu_5 - \nu_5$ ,  $\nu_5 + 2\nu_7 - 2\nu_7$ , and  $\nu_5 + \nu_6 - \nu_6$ , which lie at energies above 1100  $\text{cm}^{-1}$ , and they are all part of a complex network of resonances (Mbosei et al. 2000) that are currently under a separate investigation in greater detail. Nevertheless, our chosen cutoff enables a complete and self-consistent analysis of the bottom part of the vibrational energy manifold of  $\text{HC}_3\text{N}$ . We would also like to point out that we identified three new bands that have not yet been reported: the  $\nu_4$  stretching fundamental and the perturbation-enhanced  $\nu_4 - \nu_7$  and  $4\nu_7 - \nu_7$  bands that gain intensity from the fairly strong interactions among the energy levels  $v_4 = 1$ ,  $v_5 = v_7 = 1$ , and  $v_7 = 4$ . These levels are all around 880  $\text{cm}^{-1}$  and are connected by the purely vibrational resonance terms  $\tilde{H}_{30}$ ,  $\tilde{H}_{40}$ , and  $\tilde{H}_{50}$ . Local perturbations caused by the avoided crossing among ro-vibrational levels are clearly visible in the infrared spectrum, particularly in the  $Q$ -branch of the  $\nu_5 + \nu_7 - \nu_7$  hot band, as illustrated in Figure 4.

### 4.2. Rotational Spectrum

The rotational spectra of the ground and vibrationally excited states of  $\text{HC}_3\text{N}$  have already been investigated by several authors (see Section 1). Table 3 presents an overview of the rotational data used in the present ro-vibrational analysis with the corresponding references. Besides previous literature data, we report here a few unpublished sub-mm measurements, as well as a new set of lines recorded recently in Bologna and in Garching. These new data sets were acquired so as to work out the ambiguities that arose by

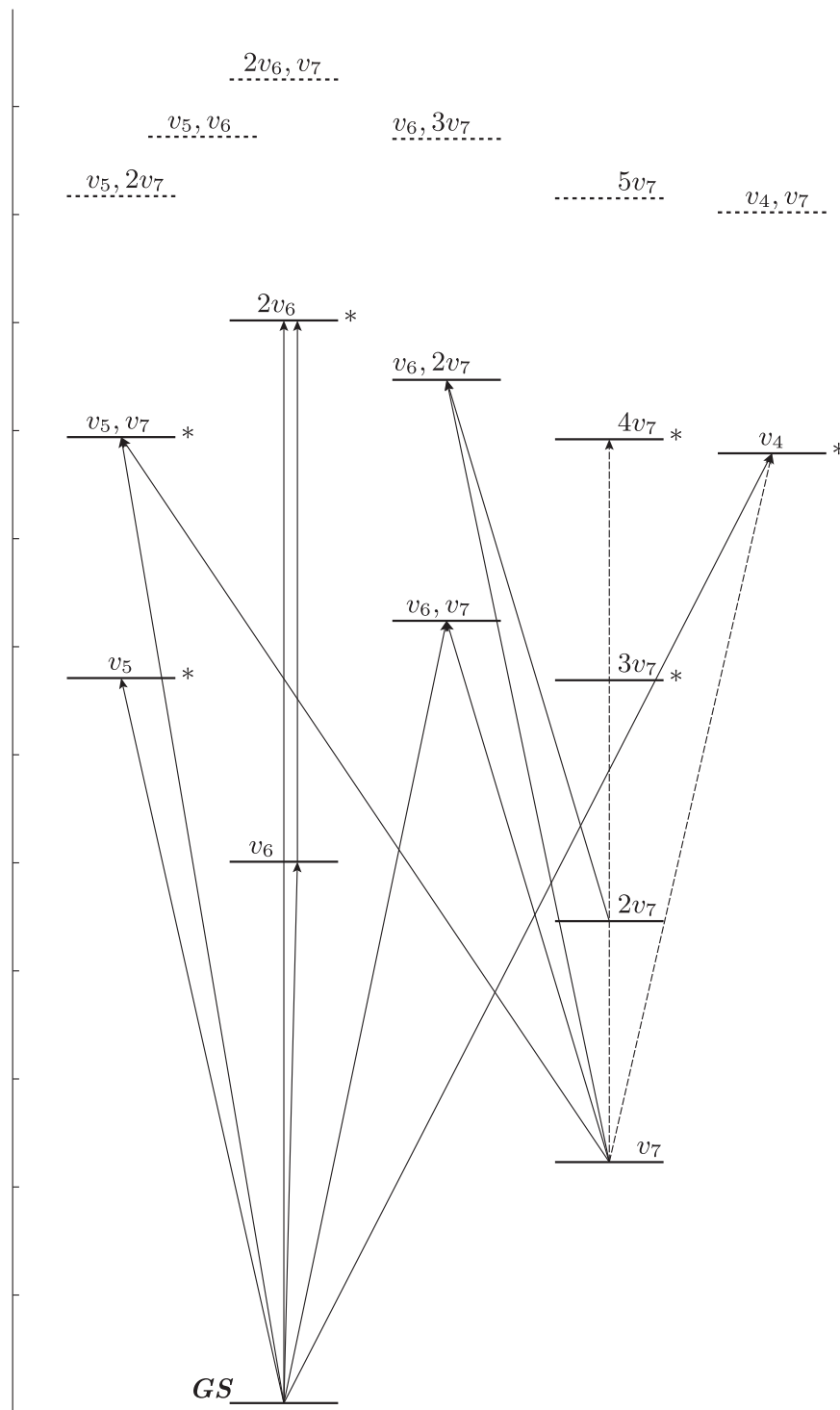


**Figure 1.** Vibrational energy-level diagram of HC<sub>3</sub>N up to  $\sim 1300\text{ cm}^{-1}$ . The states are labelled in a compact manner with the excited quanta indicated. The investigated levels are plotted with solid horizontal lines, and the arrows show the 13 IR bands analyzed. Interacting states are marked with an asterisk. The two dashed arrows indicate the perturbation-enhanced bands.

revising previous literature data (e.g., the sub-mm data reported in Mbosei et al. 2000 are often affected by large uncertainties) and to improve the frequency coverage of some coarsely sampled spectra. Maximum effort was applied to the study of the strongly interacting states  $v_5 = v_7 = 1$  and  $v_7 = 4$ , for which 300 new lines—including 28 perturbation-enhanced cross-ladder transitions—were recorded.

Figure 5 provides a hint of the complexity of the vibrationally excited spectrum of HC<sub>3</sub>N. The 1.2 GHz-long spectral scan has been recorded in the region of the  $J = 10 \leftarrow 9$  rotational transition. All of the vibrational satellites extend to the high-frequency side with respect to the ground-state line (out of scale in the plot) located at 90979 MHz. In this excerpt, the *l*-type resonance patterns of all

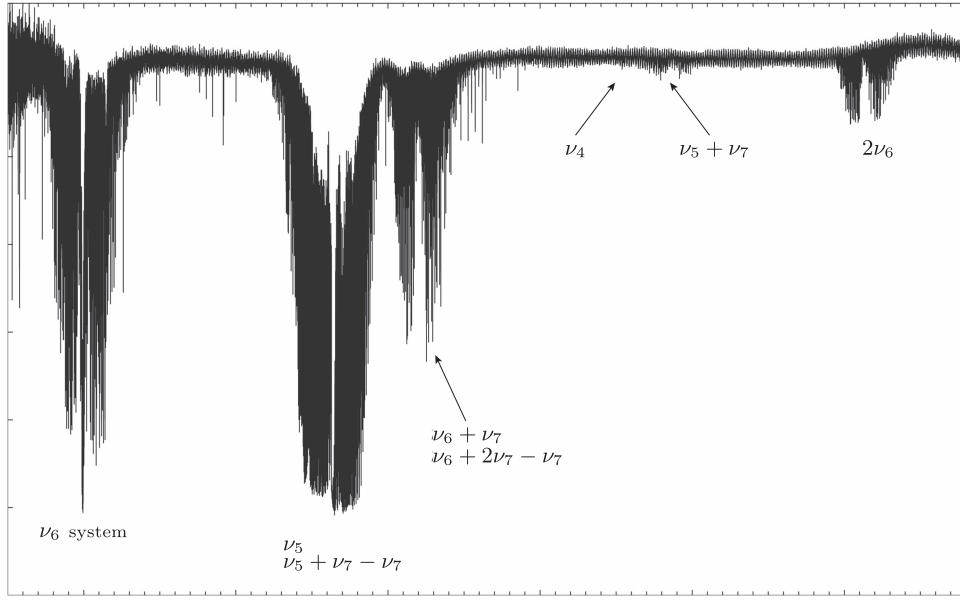


**Figure 2.** Overview of the infrared spectrum of  $\text{HC}_3\text{N}$  in the  $450\text{--}1100\text{ cm}^{-1}$  region. The analyzed bands are indicated. The  $\nu_6$  system includes the  $\nu_6 + \nu_7 - \nu_7$ ,  $2\nu_6 - \nu_6$ , and  $\nu_6 + 2\nu_7 - 2\nu_7$  hot bands. Recording conditions:  $T = 298\text{ K}$ ,  $P = 67\text{ Pa}$ ,  $L_{\text{path}} = 4\text{ m}$ , 880 scans, unapodized resolution  $0.004\text{ cm}^{-1}$ .

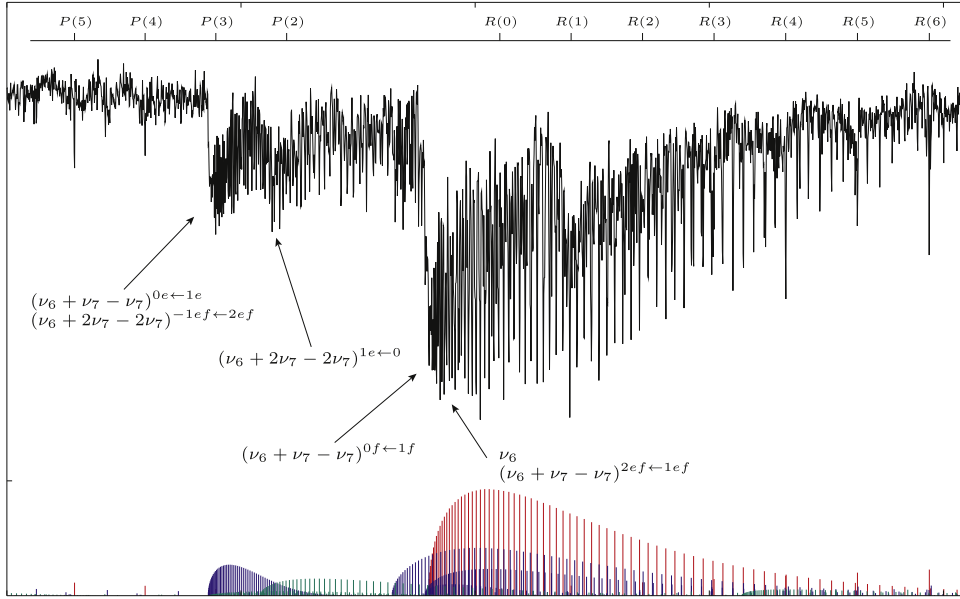


**Figure 3.** Portion of the infrared spectrum of  $\text{HC}_3\text{N}$  showing the region of the  $\nu_6$  band center. The upper axis indicates the  $P$ ,  $R$  line assignments for the fundamental  $\nu_6$  band. The stick spectrum indicates the  $\nu_6$  (red), the  $\nu_6 + \nu_7 - \nu_7$  (blue), and the  $\nu_6 + 2\nu_7 - 2\nu_7$  (green) bands. Line positions and relative intensities were calculated using the spectroscopic constants of Tables 5–8. Recording conditions:  $T = 298\text{ K}$ ,  $P = 16\text{ Pa}$ ,  $L_{\text{path}} = 4\text{ m}$ , 440 scans, unapodized resolution  $0.004\text{ cm}^{-1}$ .

of the bending excited states treated in the global analysis are visible.

## 5. Analysis

The sample of IR and pure rotational data contains about 3400 ro-vibrational lines for 13 bands plus some 1500 pure rotational lines for 12 vibrational states. The latter measurements extend over a very broad frequency interval that ranges from the radio frequencies to the THz regime. The composition and general features of the data set are summarized in Tables 2 and 3. A different weighting factor,  $w_i = 1/\sigma_i^2$ , was given to each  $i$ th datum in order to take into account the different measurement precisions  $\sigma$ .

Two different uncertainties were used for the present IR measurement:  $\sigma = 0.5 \times 10^{-3}\text{ cm}^{-1}$  for most measurements, whereas  $\sigma = 1 \times 10^{-3}\text{ cm}^{-1}$  was adopted for the very weak  $\nu_4$  and for a few other bands more affected by anharmonic resonances. A summary of the weighting scheme is reported in Table 2. For pure rotational lines, we adopted the general rule of retaining the weights used in the original works. In the cases when this information was missing, we adopted the ones provided by Yamada et al. (1995) and Thorwirth et al. (2000), who performed spectral analyses including data from the literature. As far as our new mm/sub-mm measurements are concerned, we typically adopted an uncertainty of 15 kHz. When necessary, a suitable different  $\sigma$  was used.

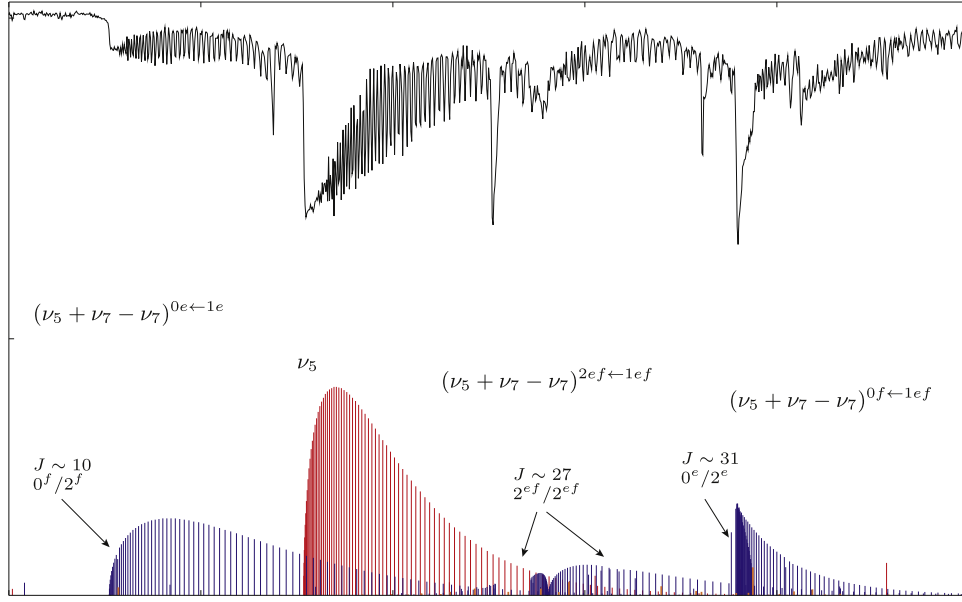


**Figure 4.** Portion of the infrared spectrum of HC<sub>3</sub>N showing the region of the  $\nu_5$  band center. The stick spectrum indicates the  $\nu_5$  (red) and the  $\nu_5 + \nu_7 - \nu_7$  (blue) bands. Sparse orange sticks mark the  $4\nu_7 - \nu_7$  lines whose intensity is enhanced by the strong  $\nu_7 = 4 \sim \nu_5 = \nu_7 = 1$  ro-vibrational mixing (see text). Local perturbations due to the level avoided crossings are apparent in the  $Q$ -branches and are indicated. The line positions and relative intensities were calculated using the spectroscopic constants of Tables 5–8. Recording conditions:  $T = 298$  K,  $P = 16$  Pa,  $L_{\text{path}} = 4$  m, 440 scans, unapodized resolution  $0.004$  cm<sup>-1</sup>.

**Table 2**  
Ro-vibrational Bands of HC<sub>3</sub>N Analyzed in This Work

Band	Sub-bands	Wav. Range (cm <sup>-1</sup> )	$P, Q, R$ ( $J_{\min} - J_{\max}$ )	No. of Lines	$\sigma_l^a$ (10 <sup>-3</sup> cm <sup>-1</sup> )
$\nu_6$	$\Pi - \Sigma^+$	477–523	$P(3-77), Q(3-83), R(2-72)$	218	0.5
$\nu_6 + \nu_7 - \nu_7$	$(\Sigma^\pm, \Delta) - \Pi$	475–528	$P(2-89), Q(3-89), R(2-91)$	647	0.5
$2\nu_6 - \nu_6$	$(\Sigma^+, \Delta) - \Pi$	479–536	$P(1-73), Q(18-73), R(1-79)$	435	0.5
$\nu_6 + 2\nu_7 - 2\nu_7$	$\Pi - (\Sigma^+, \Delta)$	474–524	$P(3-82), R(3-78)$	339	0.5
$\nu_5$	$\Pi - \Sigma^+$	632–696	$P(2-103), Q(18-78), R(0-105)$	264	0.5
$\nu_5 + \nu_7 - \nu_7$	$(\Sigma^\pm, \Delta) - \Pi$	641–691	$P(1-70), Q(4-59), R(1-91)$	623	1.0
$\nu_4 - \nu_7^*$	$\Sigma^+ - \Pi$	617–650	$P(9-65), Q(8-69), R(3-34)$	118	1.0
$4\nu_7 - \nu_7^*$	$(\Sigma^+, \Delta) - \Pi$	648–672	$P(24-50), R(25-48)$	19	1.0
$\nu_6 + \nu_7$	$\Sigma^+ - \Sigma^+$	702–746	$P(1-84), R(1-86)$	236	0.5
$\nu_4$	$\Sigma^+ - \Sigma^+$	845–877	$P(5-52), R(2-49)$	89	1.0
$\nu_5 + \nu_7$	$\Sigma^+ - \Sigma^+$	868–909	$P(1-70), R(0-64)$	131	1.0
$2\nu_6$	$\Sigma^+ - \Sigma^+$	998–1030	$P(2-78), R(1-76)$	153	0.5
$\nu_6 + 2\nu_7 - \nu_7$	$\Pi - \Pi$	706–734	$P(6-45), R(4-44)$	161	0.5

**Note.** Asterisks label perturbation-enhanced bands.

<sup>a</sup> Estimated measurement accuracy.

The spectral analysis was performed using a custom PYTHON code that uses the SPFIT program (Pickett 1991) as the computational core. All of the  $l$ -sublevels of the 12 vibrational states are simultaneously represented in a  $37 \times 37$  ro-vibrational energy matrix that is set up for each  $J$  using the Hamiltonian described in Section 3. This matrix is then reduced to a block-diagonal form, and each block is separately diagonalized to give the energy eigenvalues which are then compared to the observed ro-vibrational terms. The coefficients of the molecular Hamiltonian are optimized through an iterative least-squares procedure, which delivers effective spectroscopic constants for each individual state (Equations (4)–(9)) plus a set of resonance parameters (Equations (13)–(18)).

Actually, not all of the coefficients of the Hamiltonian terms that matter for a given vibrational state could be determined from the available experimental data. For example, in states

with  $l_l = 1$ , the  $l$ -dependent contributions expressed by the parameters  $x_{L(l)}$ ,  $d_{JL(l)}$ , and  $h_{JL(l)}$  merely produce additive terms to the corresponding  $G_v$ ,  $B_v$ , and  $D_v$  constants (see Equation (4)) and cannot be adjusted in the fit. A few other adjustable constants turned out to be ill-determined due to the correlations and were thus held fixed in the analysis. Reliable constraints for these spectroscopic parameters were obtained from the present experimental analysis: no assumptions derived from related molecules or theoretical calculations were adopted. The fixed spectroscopic constants of a given vibrational level were derived from the corresponding optimized values obtained for other levels belonging to the same vibrational manifold considering, whenever feasible, a linear  $v$ -dependence. The fitting procedure was thus repeated until convergence of these interpolated/extrapolated values was achieved.



**Table 3**  
Rotational Data of HC<sub>3</sub>N Used in the Analysis

State	$ k $	$J$ Range	Freq. Range (GHz)	No. of Lines	Reference
Ground State	0	0–117	9–1 070	76	dZ71, C77, C91, Y95, M00, T00, *
$\nu_7 = 1$	$1^{ef}$	2–112	0.039–1 038 <sup>a</sup>	111	L68, M78, dL85, Y86, C91, M00, T00, *
$\nu_7 = 2$	0, $2^{ef}$	0–100	9–923	124	M78, Y86, M00, T00, *
$\nu_7 = 3$	(1, 3) <sup>ef</sup>	2–100	27–925	146	L68, M78, Y86, M00, T00, *
$\nu_7 = 4$	0, (2, 4) <sup>ef</sup>	0–100	9–927	202	M78, Y86, *
$\nu_6 = 1$	$1^{ef}$	2–100	0.021–918 <sup>a</sup>	105	M78, dL85, Y86, M00, T00, Mor, *
$\nu_6 = 2$	0, $2^{ef}$	0–99	9–911	80	M78, Y86, M00, *
$\nu_5 = 1$	$1^{ef}$	2–100	0.015–917 <sup>a</sup>	79	dL85, M78, Y86, M00, T00, *
$\nu_4 = 1$	0	0–98	9–897	39	M78, Y86, M00, T00, *
$\nu_6 = \nu_7 = 1$	(0, 2) <sup>ef</sup>	0–100	9–922	126	Y86, M00, T00, *
$\nu_5 = \nu_7 = 1$	(0, 2) <sup>ef</sup>	0–100	9–920	211	Y86, M00, *
$\nu_6 = 1, \nu_7 = 2$	(−1, 1, 3) <sup>ef</sup>	7–99	73–914	138	Y86, M00, *
interstate		9–56	92–522	28	*

**Note.** dZ71 = de Zafra (1971), C77 = Creswell et al. (1977), C91 = Chen et al. (1991), Y95 = Yamada et al. (1995), M00 = Mbosei et al. (2000), T00 = Thorwirth et al. (2000), M78 = Mallinson & de Zafra (1978), Y86 = Yamada & Creswell (1986), L68 = Lafferty (1968), dL85 = DeLeon & Muentner (1985), Mor = Moraveć (1994). Asterisk indicates that lines from this work are also included.

<sup>a</sup> Includes MBER measurements from DeLeon & Muentner (DeLeon & Muentner 1985).

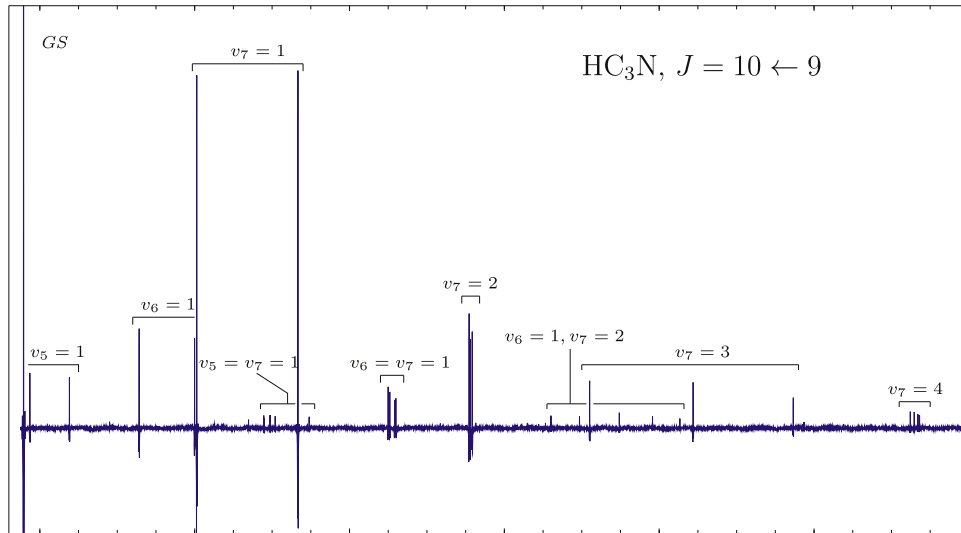


**Figure 5.** 1.2 GHz-long recording of the pure rotational spectrum of HC<sub>3</sub>N at 3 mm wavelength in the region of the  $J = 10 \leftarrow 9$  transition. The out-of-scale feature on the left is the ground-state line located at 90979 MHz. Line multiplets of nine bending excited states are visible; they are the fundamentals  $\nu_5 = 1$ ,  $\nu_6 = 1$ ,  $\nu_7 = 1$ ; the overtones  $\nu_7 = 2$ ,  $\nu_7 = 3$ , and  $\nu_7 = 4$ ; and the combinations  $\nu_5 = \nu_7 = 1$ ,  $\nu_6 = \nu_7 = 1$ , and  $\nu_6 = 1, \nu_7 = 2$ . Recording conditions:  $T = 298$  K,  $P = 0.7$  Pa, scan speed =  $2.5 \text{ MHz s}^{-1}$ , with  $RC = 3$  ms.

The list of the analyzed transition frequencies/wavenumbers, including the least-squares residuals and the estimated measurement uncertainties, is provided as digital supporting data. An excerpt is presented here in Table 4 for guidance. The data is also available in the Cologne Database for Molecular Spectroscopy (Endres et al. 2016). The spectroscopic parameters resulting from the global fit procedure are gathered in Tables 5–8. Some details concerning the analysis are given in the following subsections.

### 5.1. Isolated States

Some of the bands considered in the analysis do not show any evidence of perturbation; the involved vibrational states were thus considered isolated. They are the ground state, the  $\nu_6 = 1$  and  $\nu_7 = 1$ , the  $\nu_7 = 2$ , and the  $\nu_6 = \nu_7 = 1$  and  $\nu_6 = 1, \nu_7 = 2$  bend–bend combination states. Experimental

information about these excited states derive from the measurements of several IR bands, namely,  $\nu_6$ ,  $\nu_6 + \nu_7$ ,  $\nu_6 + \nu_7 - \nu_7$ ,  $\nu_6 + 2\nu_7 - \nu_7$ , and  $\nu_6 + 2\nu_7 - 2\nu_7$  (see Table 2). This rich set of data makes it possible to derive accurate vibrational energies for all the states, including the  $\nu_7 = 1$  and  $\nu_7 = 2$  bending levels, even if the  $\nu_7$  fundamental and  $2\nu_7$  overtone bands were not directly observed.

The pure rotational data available for these vibrational states include meter-wave molecular beam electric resonance measurements (MBER), direct  $l$ -type measurements at cm wavelength, and rotational spectra up to the THz regime (see Table 3 for the bibliographic references). For the ground state, we recorded a few high- $J$  lines located above 1 THz in order to improve the determination of the quartic ( $D_0$ ) and sextic ( $H_0$ ) centrifugal distortion constants, and a subset of very precise ( $\sigma = 2$  kHz) measurements at 3 mm. For the  $\nu_6 = 1, \nu_7 = 2$

**Table 4**  
Measured Line Positions and Least-squares Residuals for HC<sub>3</sub>N

$J'$	$l'_5$	$l'_6$	$l'_7$	$k'$	$\leftarrow$	$J$	$l_5$	$l_6$	$l_7$	$k$	Observed	Residual	$\sigma^a$	Units	References
...															
$v_7 = 4$															
8	0	0	0	0 <sup>e</sup>		7	0	0	0	0 <sup>e</sup>	73702.486	0.00009	0.020	MHz	Y86
9	0	0	0	0 <sup>e</sup>		8	0	0	0	0 <sup>e</sup>	82913.690	-0.00521	0.015	MHz	TW
10	0	0	0	0 <sup>e</sup>		9	0	0	0	0 <sup>e</sup>	92124.342	0.00161	0.015	MHz	TW
11	0	0	0	0 <sup>e</sup>		10	0	0	0	0 <sup>e</sup>	101334.352	-0.00760	0.015	MHz	TW
12	0	0	0	0 <sup>e</sup>		11	0	0	0	0 <sup>e</sup>	110543.700	0.00857	0.020	MHz	Y86
...															
$v_5 + v_7 - v_7$															
20	1	0	1	2 <sup>e</sup>		21	0	0	1	1 <sup>e</sup>	657.39883	0.00006	0.001	cm <sup>-1</sup>	TW
21	1	0	1	2 <sup>e</sup>		22	0	0	1	1 <sup>e</sup>	657.10124	0.00029	0.001	cm <sup>-1</sup>	TW
22	1	0	1	2 <sup>e</sup>		23	0	0	1	1 <sup>e</sup>	656.80393	0.00011	0.001	cm <sup>-1</sup>	TW
23	1	0	1	2 <sup>e</sup>		24	0	0	1	1 <sup>e</sup>	656.50797	0.00016	0.001	cm <sup>-1</sup>	TW
24	1	0	1	2 <sup>e</sup>		25	0	0	1	1 <sup>e</sup>	656.21416	0.00019	0.001	cm <sup>-1</sup>	TW
25	1	0	1	2 <sup>e</sup>		26	0	0	1	1 <sup>e</sup>	655.92520	0.00025	0.001	cm <sup>-1</sup>	TW
...															

**Note.** Y86 = Yamada & Creswell (1986), TW = this work.

<sup>a</sup> Assumed uncertainty for statistical weight calculation (see the text).

(This table is available in its entirety in machine-readable form.)

**Table 5**  
Results of the Ro-vibrational Analysis Performed for HC<sub>3</sub>N: Ground and Singly Excited States

Parameter	Units	GS	$v_4 = 1$	$v_5 = 1$	$v_6 = 1$	$v_7 = 1$
$G_v$	cm <sup>-1</sup>	...	878.312(17)	663.368484(31)	498.733806(26)	221.838739(33)
$x_{L(tt)}$	GHz	...	...	0.0 <sup>a</sup>	6.59 <sup>b</sup>	21.7972 <sup>b</sup>
$y_{L(tt)}$	MHz	...	...	0.0 <sup>a</sup>	0.0 <sup>a</sup>	-2.10 <sup>b</sup>
$B_v$	MHz	4549.058614(30)	4538.0977(21)	4550.62412(17)	4558.301481(60)	4563.525640(61)
$D_v$	kHz	0.5442578(96)	0.545383(83)	0.545852(25)	0.554436(10)	0.568004(10)
$H_v$	mHz	0.0509(12)	0.0378(20)	0.0509(12)	0.06450(57)	0.10468(52)
$L_v$	nHz	-0.329(42)	-0.329 <sup>b</sup>	-0.329 <sup>b</sup>	-0.329 <sup>b</sup>	-0.329 <sup>b</sup>
$d_{JL(tt)}$	kHz	...	...	0.0 <sup>a</sup>	12.75 <sup>b</sup>	-12.287 <sup>b</sup>
$h_{JL(tt)}$	Hz	...	...	0.0 <sup>a</sup>	0.0 <sup>a</sup>	0.2443 <sup>b</sup>
$l_{JL(tt)}$	$\mu$ Hz	...	...	0.0 <sup>a</sup>	0.0 <sup>a</sup>	-0.274 <sup>b</sup>
$q_t$	MHz	...	...	2.53870(11)	3.5821947(42)	6.5386444(58)
$q_{tJ}$	Hz	...	...	-1.3382(75)	-2.0611(20)	-16.2870(43)
$q_{tJJ}$	mHz	...	...	0.0 <sup>a</sup>	0.0 <sup>a</sup>	56.98(33)

**Notes.** The numbers in parentheses are the  $1\sigma$  uncertainties expressed in units of the last quoted digit.

<sup>a</sup> Constrained.

<sup>b</sup> Assumed value, held fixed in the fit (see the text).

bend-bend combination state, less extensive rotational data were available. We thus carried out new measurements in the 270–700 GHz frequency range in order to achieve a satisfactory  $J$  sampling to accurately model the  $l$ -type resonance effects.

Highly precise values for the rotational ( $B_v$ ) and the quartic ( $D_v$ ) centrifugal distortion constants were obtained for all of the states. The derived  $1\sigma$  standard errors of the  $B_v$  parameters are a few tens of Hz (140 Hz for  $v_6 = 1$ ,  $v_7 = 2$ ), while those of  $D_v$  are of the order of 0.1 mHz or better. We obtained a well-determined (12%) estimate for the octic centrifugal distortion constant ( $L_v$ ) for the ground state, and the sextic constants ( $H_v$ ) were determined for all of the states with good precision (0.5%–5%). These values show a very smooth linear dependence on the vibrational quantum numbers  $v_6$  and  $v_7$ .

Even vibrational trends are also observed for some high-order  $l$ -type parameters, such as  $q_J$ ,  $r_J$ ,  $u_{67}$ . Anomalies in the fitted values of these small coefficients are very sensitive

indicators of spectral perturbations, hence the observed regular behavior allow us to rule out various interaction terms. They are the Coriolis-type  $\tilde{H}_{31}$ , which accounts for the  $v_6 = 1 \sim v_7 = 2$  and  $v_5 = 1 \sim v_6 = v_7 = 1$  couplings, and the anharmonic  $\tilde{H}_{40}$  producing the  $v_5 = 2 \sim v_6 = v_7 = 1$  interaction. These resonances were considered by Fayt et al. (2004a, 2008) in the global analysis of the HCCC<sup>15</sup>N but they proved to be negligible for HC<sub>3</sub>N in the  $J$  range sampled in the present investigation.

### 5.2. The Interacting States $v_5 = 1 \sim v_7 = 3$

The  $v_5 = 1$  is the highest-energy bending fundamental (H–C≡C) and is located  $\sim 663$  cm<sup>-1</sup> above the ground state. This state has a  $\Pi$  symmetry and can interact with the  $l_7 = 1$  level ( $\Pi$  symmetry) of the nearby  $v_7 = 3$  manifold. The vibrational harmonic energy difference between these two states is  $\omega_5 - 3\omega_7 \simeq -17.9$  cm<sup>-1</sup> (G. Pietropolli Charmet

**Table 6**  
Results of the Ro-vibrational Analysis Performed for HC<sub>3</sub>N: Overtone Bending States

Parameter	Units	$v_6 = 2$	$v_7 = 2$	$v_7 = 3$	$v_7 = 4$
$G_v$	cm <sup>-1</sup>	997.913(17)	442.899036(61)	663.2205(29)	882.85147(21)
$x_{L(u)}$	GHz	6.59(13)	21.62866(55)	21.4398(12)	21.2814(15)
$y_{L(u)}$	MHz	0.0 <sup>a</sup>	-2.10 <sup>b</sup>	-2.10 <sup>b</sup>	-2.100(75)
$B_v$	MHz	4567.4528(17)	4577.966834(78)	4592.38340(20)	4606.77431(27)
$D_v$	kHz	0.564556(14)	0.5922476(90)	0.617092(43)	0.642476(16)
$H_v$	mHz	0.07607(75)	0.15789(43)	0.2103(16)	0.27016(88)
$L_v$	nHz	-0.329 <sup>b</sup>	-0.329 <sup>b</sup>	-0.329 <sup>b</sup>	-0.329 <sup>b</sup>
$d_{JL(u)}$	kHz	12.75(41)	-13.116(23)	-14.002(26)	-14.803(17)
$h_{JL(u)}$	Hz	0.0 <sup>a</sup>	0.2035(16)	0.1433(72)	0.1122(16)
$l_{JL(u)}$	μHz	0.0 <sup>a</sup>	-1.261 <sup>b</sup>	-2.25(24)	-3.235(96)
$q_t$	MHz	3.582195 <sup>b</sup>	6.563988(58)	6.587477(36)	6.612440(40)
$q_{tJ}$	Hz	-2.0611 <sup>b</sup>	-16.5793 <sup>b</sup>	-16.872(10)	-17.3008(98)
$q_{tJJ}$	mHz	0.0 <sup>a</sup>	54.31 <sup>b</sup>	51.64(64)	56.96(56)
$u_{tt}$	Hz	...	-0.1829 <sup>b</sup>	-0.1506(42)	-0.11825(50)

**Notes.** The numbers in parentheses are the  $1\sigma$  uncertainties expressed in units of the last quoted digit.

<sup>a</sup> Constrained.

<sup>b</sup> Assumed value, held fixed in the fit (see the text).

**Table 7**  
Results of the Ro-vibrational Analysis Performed for HC<sub>3</sub>N: Bend-Bend Combination States

Parameter	Units	$v_5 = v_7 = 1$	$v_6 = v_7 = 1$	$v_6 = 1, v_7 = 2$
$G_v$	cm <sup>-1</sup>	885.37215(63)	720.293173(30)	941.070371(59)
$x_{L(u)}$	GHz	0.0 <sup>a</sup>	6.59 <sup>b</sup>	6.59 <sup>b</sup>
$x_{L(77)}$	GHz	21.7972 <sup>b</sup>	21.7256 <sup>b</sup>	21.6541(11)
$x_{L(77)}$	GHz	19.277(20)	17.12595(41)	17.12142(89)
$y_{L(77)}$	MHz	-2.10 <sup>b</sup>	-2.10 <sup>b</sup>	-2.10 <sup>b</sup>
$r_{77}$	GHz	6.999(39)	-11.77173(62)	-11.4965(12)
$r_{77J}$	kHz	-0.0252(14)	-12.670(74)	-10.205(90)
$r_{77JJ}$	Hz	1.117(88)	2.029(96)	2.047(23)
$B_v$	MHz	4565.08511(80)	4572.861121(64)	4587.39057(14)
$D_v$	kHz	0.569558(21)	0.578017(11)	0.6021526(97)
$H_v$	mHz	0.10346(64)	0.12639(62)	0.18979(54)
$L_v$	nHz	-0.329 <sup>b</sup>	-0.329 <sup>b</sup>	-0.329 <sup>b</sup>
$d_{JL(u)}$	kHz	0.0 <sup>a</sup>	12.75 <sup>b</sup>	12.75 <sup>b</sup>
$d_{JL(77)}$	kHz	-12.287 <sup>b</sup>	-9.408 <sup>b</sup>	-6.529(50)
$h_{JL(77)}$	Hz	0.2443 <sup>b</sup>	0.2443 <sup>b</sup>	0.2035 <sup>b</sup>
$l_{JL(77)}$	μHz	-0.274 <sup>b</sup>	-0.274 <sup>b</sup>	-1.261 <sup>b</sup>
$d_{JL(77)}$	kHz	-21.22(61)	55.700(84)	50.580(42)
$h_{JL(77)}$	Hz	1.03(10)	0.0 <sup>a</sup>	0.0 <sup>a</sup>
$q_t$	MHz	2.56538(23)	3.62324(50)	3.67072(44)
$q_{tJ}$	Hz	-1.4356(88)	-2.2429 <sup>b</sup>	-2.426(10)
$q_7$	MHz	6.53864 <sup>b</sup>	6.59341(21)	6.61796(19)
$q_{7J}$	Hz	-16.287 <sup>b</sup>	-16.386(11)	-16.6165(70)
$q_{7JJ}$	mHz	57.0 <sup>b</sup>	57.0 <sup>b</sup>	54.3 <sup>b</sup>
$u_{77}$	Hz	...	...	-0.1854(36)
$u_{77}$	Hz	-1.14(11)	-2.211(98)	-2.259(24)
$q_{677}$	kHz	...	...	-14.548(99)

**Notes.** The numbers in parentheses are the  $1\sigma$  uncertainties expressed in units of the last quoted digit.

<sup>a</sup> Constrained.

<sup>b</sup> Assumed value, held fixed in the fit (see the text).

2017, in preparation). The anharmonic value, which can be obtained from our experimental data, is  $G_{v_5} - G_{3v_7} - x_{L(77)} \simeq -0.57$  cm<sup>-1</sup>. The two states are actually closely degenerate and can be coupled by the  $\tilde{H}_{40}$  term of the effective Hamiltonian whose matrix elements are given in Equation (15). Both  $e$  and  $f$  parity sublevels are affected by contributions of similar magnitude. Due to the small value of the  $C_{40}$  quartic

coefficient, the resonance is weak: at low values of the  $J$  quantum number, where the effects are stronger, each ro-vibrational level is pushed away by  $\approx 60$  MHz. The resonance strength decreases with increasing  $J$  because the upper level,  $v_7 = 3$ , has a higher value of the rotational constant  $B_v$ , and therefore the two interacting states become more and more separate in energy with the rotational excitation.

**Table 8**  
Results of the Ro-vibrational Analysis Performed for HC<sub>3</sub>N:  
Resonance Parameters

Interacting States	Parameter	Units	Fitted Value
$(\nu_5 = 1) - (\nu_7 = 3)$	$C_{40}$	MHz	784.4(42)
	$C_{42}^J$	kHz	-29.1(37)
$(\nu_5 = \nu_7 = 1) - (\nu_7 = 4)$	$C_{40}$	MHz	747.1(43)
	$C_{42}^J$	MHz	0.1276(56)
	$C_{42a}$	kHz	20.31(70)
	$C_{42b}$	kHz	7.86(42)
$(\nu_4 = 1) - (\nu_6 = 2)$	$C_{30}$	cm <sup>-1</sup>	16.0275(81)
	$C_{32}^J$	MHz	-0.5164(20)
$(\nu_4 = 1) - (\nu_5 = \nu_7 = 1)$	$C_{30}$	cm <sup>-1</sup>	-2.4161(34)
$(\nu_4 = 1) - (\nu_7 = 4)$	$C_{50}$	GHz	3.458(24)
	$C_{52}^J$	kHz	34.2(12)

**Note.** The numbers in parentheses are the  $1\sigma$  uncertainties expressed in units of the last quoted digit.

Experimental information about these interacting states are provided by the  $\nu_5$  band recorded in the IR (see Table 2) and by the pure rotational spectra for the vibrationally excited  $\nu_5 = 1$  and  $\nu_7 = 3$  states. The ro-vibrational data allow an accurate determination of the vibrational energy of the  $\nu_5 = 1$  state, while the analysis of the resonance provides the absolute position of the  $\nu_7 = 3$  level, which is determined with a standard error of  $3 \times 10^{-3}$  cm<sup>-1</sup>.

The present set of data is not sensitive to the value of the  $x_{L(55)}$  anharmonicity constant that merely acts as an additive term to the  $\nu_5 = 1$  vibrational energy. Its value was fixed to zero, and its contribution is thus included in the corresponding  $G_v$ . The same applies to the  $d_{JL(55)}$ ,  $h_{JL(55)}$ , and  $l_{JL(55)}$  coefficients expressing the  $l$  dependency of the rotational ( $B_v$ ), quartic ( $D_v$ ), and sextic ( $H_v$ ) centrifugal distortion constants.

For  $\nu_7 = 3$ , we adjusted all of the Hamiltonian coefficients given in Equations (4) and (6), except  $y_{L(77)}$ , which was held fixed at the value derived for the  $\nu_7 = 4$  bending level (see Section 5.3). For this state, we also optimized the  $|\Delta_k| = 4$  parameter  $u_{77}$  that models high-order  $l$ -type resonance effects between the  $l_7 = 1$  and  $l_7 = 3$  sublevels. Its value was determined with a 3% standard uncertainty and its order of magnitude is in agreement with what is expected (see Section 6). Precise determinations were also obtained for  $H_v$  (0.5%) as well as other high-order parameters such as  $q_{uJJ}$  (1%),  $h_{JL(77)}$  (4%), and  $l_{JL(77)}$  (7%).

The resonance effects were modeled by adjusting the main parameter  $C_{40}^{(5777)}$  together with its  $J$ -dependence coefficient  $C_{42}^{(5777J)}$ , which was determined with a precision of about 10%. The latter, small parameter is necessary to reproduce the rotational mixing between  $\nu_5 = 1$ ,  $l_5 = 1$  and  $\nu_7 = 3$ ,  $l_7 = 1$  substates and its trend over the fairly large  $J$  interval (2–100) sampled by the present experimental data.

### 5.3. The Resonance

System  $\nu_4 = 1 \sim \nu_5 = \nu_7 = 1 \sim \nu_6 = 2 \sim \nu_7 = 4$

In HC<sub>3</sub>N, there is a polyad of interacting states which pivots on the lowest energy  $\nu_4 = 1$  stretching fundamental located at  $\sim 878$  cm<sup>-1</sup>. This state can be coupled with the  $\Sigma$  ( $l = 0$ ) sublevel of any nearby doubly excited bending state through

cubic anharmonic resonances generated by the  $\tilde{H}_{30}$  term of the effective Hamiltonian. In our analysis, we considered the interactions of  $\nu_4 = 1$  with  $\nu_5 = \nu_7 = 1$  and with  $\nu_6 = 2$ , which are located at 885 cm<sup>-1</sup> and 998 cm<sup>-1</sup>, respectively. Furthermore, the  $\nu_5 = \nu_7 = 1$  bend–bend combination state is coupled to the  $\nu_7 = 4$  level through the  $\tilde{H}_{40}$  quartic anharmonic resonance. This dyad is analogous to the one described in Section 5.2 and is obtained by adding one  $\nu_7$  quantum to the fundamental dyad  $\nu_5 = 1 \sim \nu_7 = 3$ . Finally, the weak quintic ( $\tilde{H}_{50}$ ) resonance connecting  $\nu_4 = 1$  and the  $l = 0$  sublevel ( $\Sigma$  symmetry) of the  $\nu_7 = 4$  bending state was also considered.

The detailed scheme of the energy-level manifolds involved in this resonance system is depicted in Figure 6. A major energy displacement ( $\sim 16$  cm<sup>-1</sup>) is experienced by the  $\nu_4 = 1$  (pushed down) and  $\nu_6 = 2$ ,  $l = 0$  substates (pushed up), because of the large value of the  $\phi_{466}$  cubic force constant involved in the  $\tilde{H}_{30}$  resonance term. This effect is analogous to the Fermi resonance in triatomic molecules and is also present in many linear polyatomic molecules, such as the HC<sub>3</sub>N isomer isocyanoacetylene (HCCNC; Vigouroux et al. 2000), the isoelectronic species diacetylene (HC<sub>4</sub>H; Bizzocchi et al. 2011), and the longer chain HC<sub>5</sub>N (Degli Esposti et al. 2005). Though closer in energy to  $\nu_4 = 1$ , the  $\nu_5 = \nu_7 = 1$  state is less affected by this resonance because the corresponding  $\phi_{457}$  cubic force constant is smaller. Nonetheless, the resulting displacement of  $\sim 1$  cm<sup>-1</sup> is enough to invert the relative positions of the  $k = 0^e$  and  $k = 2^e$  sublevels, altering completely the  $l$ -type resonance effects within the  $\nu_5 = \nu_7 = 1$  manifold.

As shown in Figure 6, the two interacting states  $\nu_5 = \nu_7 = 1$  and  $\nu_7 = 4$  are very close. For  $J = 2$ , the energy difference is  $\sim 3.7$  cm<sup>-1</sup> for  $0^e$  and  $\sim 1.1$  cm<sup>-1</sup> for the  $2^e$  sublevels. These gaps decrease for increasing  $J$ , because the  $\nu_7 = 4$  ro-vibrational levels—initially located below the corresponding  $\nu_5 = \nu_7 = 1$  ones—have a higher effective rotational constant ( $B_{\nu_7=4} - B_{\nu_5=\nu_7=1} \simeq 42$  MHz). The reduced frequency plot for these two states is presented in Figure 7. Deviations from linear behavior are due to high-order effects: regular, slightly bent parabolas are produced by residual energy contributions depending on  $J^6$  and produced by  $l$ -type resonances. Abrupt changes in curvature and discontinuities are generated by avoided crossings between close degenerate levels. These effects are very visible at  $J \sim 26$ –27 and  $J \sim 56$ , where almost exact degeneracies occur between the  $2^e/2^f$  and  $0^e/0$  sublevels of the two states. The lines show displacements as large as  $\sim 3$  GHz with respect to their unperturbed positions and, because of the strong ro-vibrational mixing, a series of cross-ladder (interstate) transitions gain enough intensity to be readily detected. These forbidden transitions are indicated by purple stars in Figure 7. Less striking perturbations also occur at  $J \sim 9$  ( $0^f/2^f$  crossing) and  $J \sim 48$  ( $2^e/0$  crossing).

For the states involved in this resonance system, we have a great deal of experimental information. In the IR, we recorded the  $\nu_4$ ,  $\nu_5 + \nu_7$ , and  $2\nu_6$  bands that provide the energy position of the interacting levels. Additional ro-vibrational information on all of the  $l$ -sublevels come from the measurements of the  $2\nu_6 - \nu_6$  and from the  $\nu_4 - \nu_7$  and  $4\nu_7 - \nu_7$  difference bands (see Table 2). The latter are weak IR features whose intensity is enhanced by the ro-vibrational mixing produced by the  $\tilde{H}_{30}$  and  $\tilde{H}_{40}$  resonance terms. An extensive pure rotational data set is also available for all four states given by previous and new measurements (see Table 3). The data span a remarkable  $J$

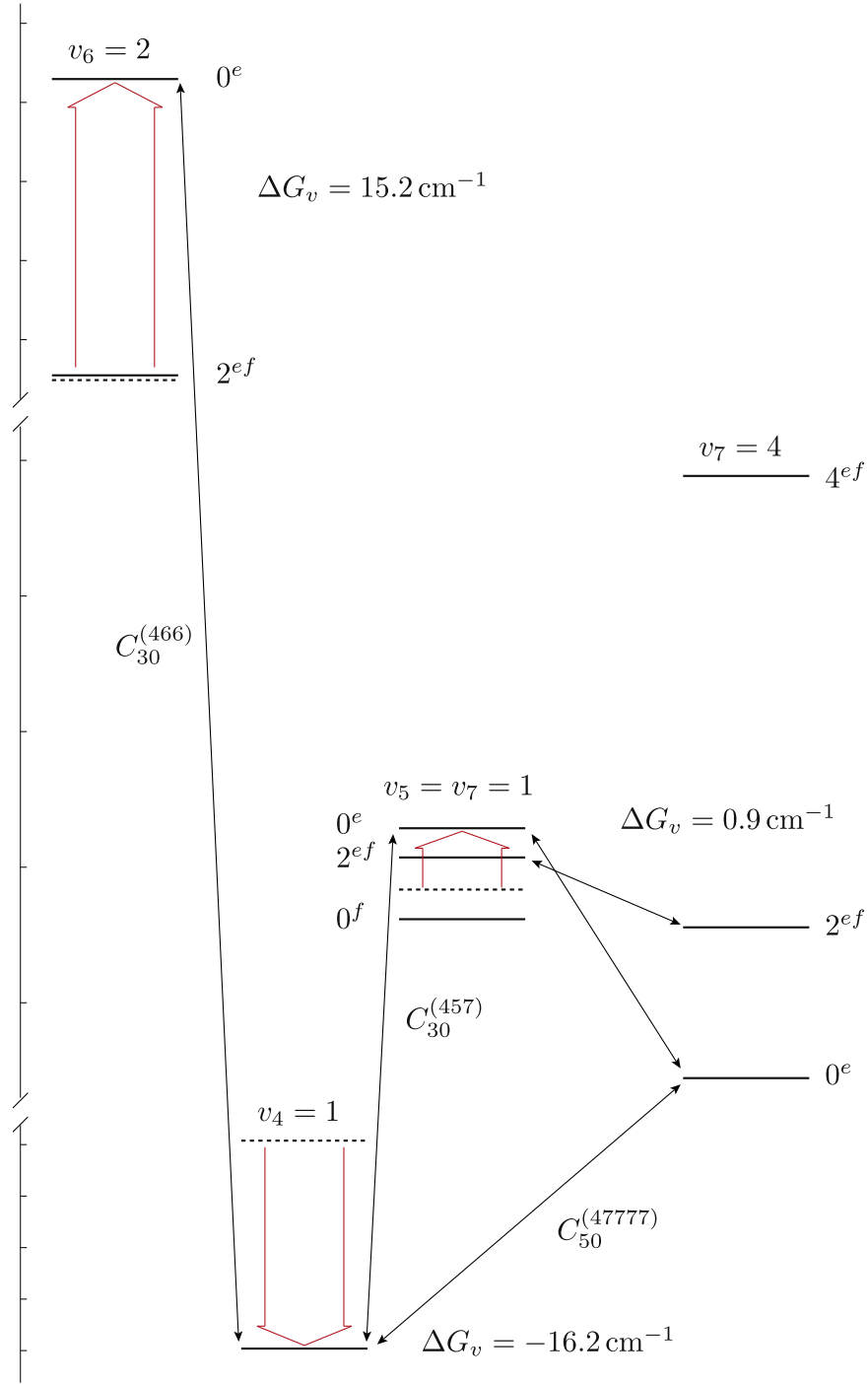


**Figure 6.** Vibrational energy-level diagram for the interacting states  $v_4 = 1$ ,  $v_5 = v_7 = 1$ ,  $v_6 = 2$ , and  $v_7 = 4$  of HC<sub>3</sub>N. Thin arrows (black) indicate the main vibrational coupling taken into account. Large arrows (red) illustrate the vibrational energy displacements produced by the anharmonic resonances; the hypothetical unperturbed level positions are plotted with dashed lines. The weak  $\Delta k = \pm 2$  interactions produced by the  $\tilde{H}_{42}$  effective Hamiltonian term between the  $v_5 = v_7 = 1$  and  $v_7 = 4$  states are not indicated.

interval, from 0 to 100, covering the 9–920 GHz frequency range. In particular, we recorded 300 new lines for the pair of states  $v_5 = v_7 = 1/v_7 = 4$ , including 28 interstate transitions around the most perturbed  $J$  values. This wealth of data enabled a complete analysis of the resonance system without using any assumption derived from theoretical calculations or extrapolated from related molecules. The absolute vibrational energy positions of all levels and most of the Hamiltonian coefficients were adjusted in the least-squares fit. In a few cases, they were

held fixed to suitable values derived from related vibrational states.

The sextic centrifugal distortion constant ( $H_v$ ) was determined for all states with good precision (7% at least). The lines of the most perturbed  $v_5 = v_7 = 1$  and  $v_7 = 4$  states required a few additional high-order parameters in order to be fitted within experimental uncertainties. Besides the  $|\Delta k| = 4$  coefficients  $u_{57}$  and  $u_{77}$ , for  $v_7 = 4$ , we had to adjust  $y_{L(77)}$ , which represents the  $l^4$  dependence of the vibrational energy and the



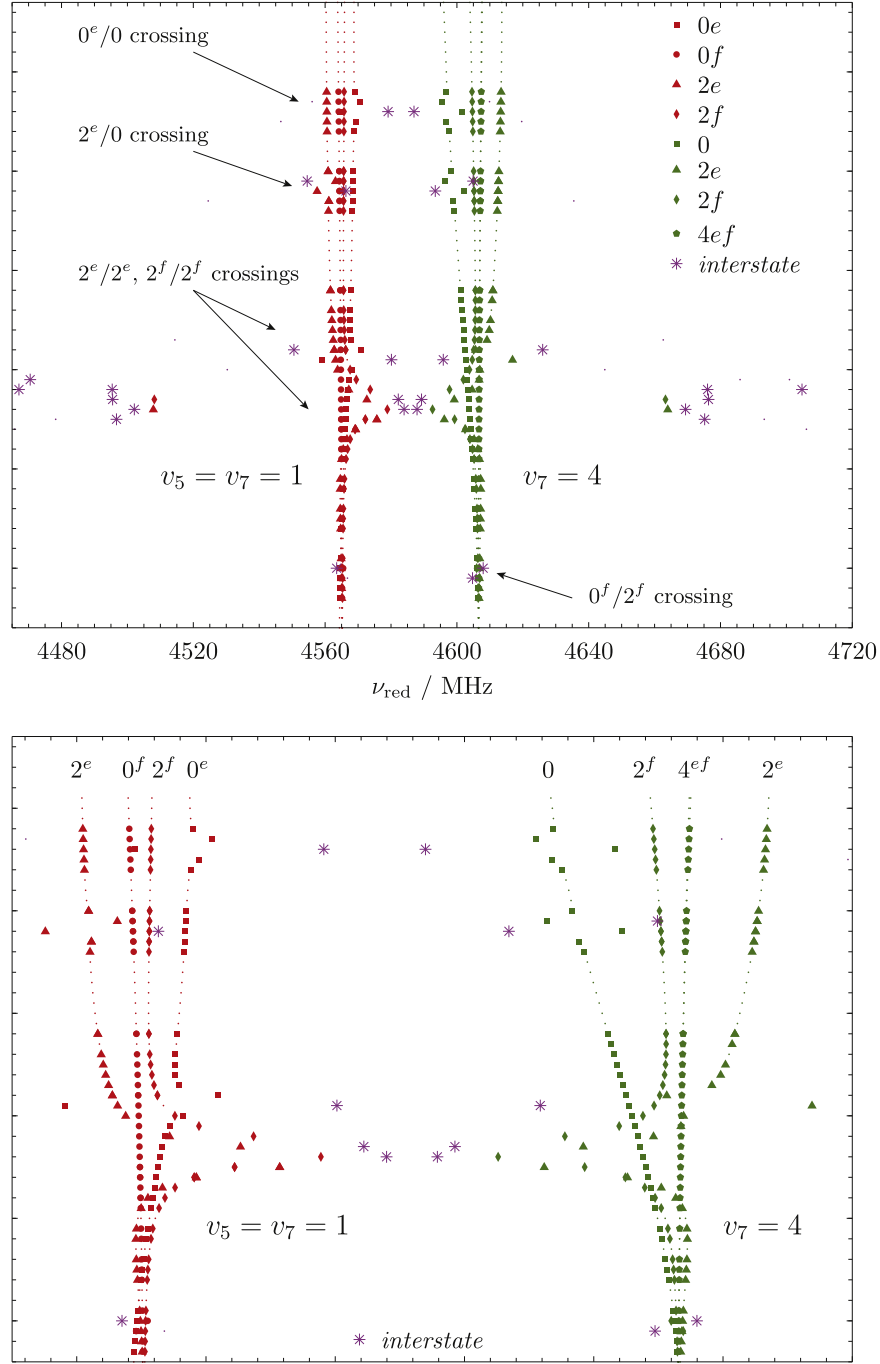


**Figure 7.** Reduced frequency diagram for the  $v_5 = v_7 = 1$  (red symbols) and  $v_7 = 4$  (green symbols) interacting states of  $\text{HC}_3\text{N}$ . The quantity plotted on the  $x$ -axis is  $\nu_{\text{red}} = [\nu + 4D(J+1)^3]/2(J+1)$ . Solid symbols denote experimental values, whereas small dots indicate calculated values based on the parameters of Tables 5–8. The most perturbed transitions, in the proximity of the crossings, are labelled using the method implemented in the SPFIT code (Pickett 1991). The bottom panel shows a detail of the upper plot in the  $\nu_{\text{red}}$  range from 4555 to 4620 MHz, and most of the interstate transitions are not visible here.

high-order  $l$ -type doubling constant  $q_{677}$  (see Equation (7)). The resonance effects were accurately modeled by including the  $J$ -dependent coefficients  $C_{32}^{(457J)}$ ,  $C_{32}^{(466J)}$ ,  $C_{42}^{(5777J)}$ , and  $C_{52}^{(47777J)}$ , plus the  $|\Delta k| = 2$  parameters  $C_{42a}^{(5777)}$ ,  $C_{42b}^{(5777)}$ .

The contribution of these terms is very small since their order of magnitude is between  $\kappa^3\omega_{\text{vib}}$  and  $\kappa^5\omega_{\text{vib}}$ , as described in Table 1. Nevertheless, their inclusion in the analysis is justified by the following considerations: (i) the wide  $\nu$  and  $J$  ranges sampled ( $J_{\text{max}} = 100$ ,  $\nu_{\text{max}} = 4$ ), (ii) the “exact” resonance occurring between the  $v_5 = v_7 = 1$  and  $v_7 = 4$  ro-vibrational levels, and (iii) the high-precision frequency

determination ( $\sigma = 15$  kHz) of the most perturbed lines and of the interstate transitions, which are extremely sensitive to subtle resonance effects.

## 6. Discussion

In the present spectral analysis, we treated simultaneously the whole set of high-resolution data available for  $\text{HC}_3\text{N}$  up to an energy of circa  $1000\text{ cm}^{-1}$ . Almost 5000 experimental transitions were included in the least-squares fit: this resulted in the determination of 11 vibrational energies and 110 spectroscopic

constants for 12 states. The overall quality of the analysis is expressed by the weighted root mean square deviation, defined as

$$\sigma_{\text{rms}} = \sqrt{\frac{1}{N} \sum_{i=1}^N \left( \frac{\nu_i^{\text{exp}} - \nu_i^{\text{calc}}}{\sigma_i} \right)^2}. \quad (19)$$

We obtained  $\sigma_{\text{rms}} = 0.875$ , indicating that the experimental data set was reproduced well within the estimated measurements accuracies.

The knowledge of the ro-vibrational spectrum of HC<sub>3</sub>N is greatly improved. The most important spectroscopic constants were determined with very high precision:  $1\sigma$  uncertainties of circa one part over  $10^8$  were obtained for the rotational constant  $B_v$  of most states, whereas the average precision of the quartic centrifugal distortion constant ( $D_v$ ) and  $l$ -type doubling constant ( $q_v$ ) is a few parts over  $10^5$  and  $10^7$ , respectively. Several anharmonicity constants of the type  $x_{L(ii)}$ ,  $x_{L(ii')}$ , and  $r_{ii'}$ , plus a number of high-order ro-vibrational parameters were also determined with good precision.

Unlike some extensive studies published in the past (e.g., Arie et al. 1990; Mbosei et al. 2000), we considered explicitly the  $l$ -type resonance effects among bending sublevels, thus obtaining a unique set of spectroscopic parameters for each vibrational state. More importantly, by joining high-resolution IR data and pure rotational measurements, we attained a thorough modeling of the spectral perturbations produced by the anharmonic resonances in the bottom part of the vibrational energy manifold of HC<sub>3</sub>N. Compared with the previous work of Yamada & Creswell (1986), who performed a similar treatment on a much more limited data set, we achieved a substantial improvement in terms of completeness of the analysis and overall accuracy of the derived spectroscopic parameters.

It should be noted that Jolly et al. (2007) performed a global treatment of all the data available for HC<sub>3</sub>N in their work. Their analysis was used to support accurate calculations of the integrated IR intensity for the  $\nu_5$  and  $\nu_6$  hot band systems, but the complete results and the list of the derived spectroscopic parameters were not published. Our study is thus the first complete ro-vibrational analysis for HC<sub>3</sub>N presented so far: the level of detail adopted in the description of the ro-vibrational energies and the wide  $J$  interval spanned by the data set make our analysis particularly suited for astrophysical applications.

### 6.1. Molecular Parameters

The methodology used for the present analysis implies the determination of one set of effective spectroscopic constants for each vibrational state, plus a few resonance parameters describing the various anharmonic couplings. In this approach, the use of a ro-vibrational Hamiltonian that includes all of the relevant interactions is critical to obtain state-specific parameters with clear physical meaning and reliable predictions for the unexplored spectral regions. Indications of the validity of such a treatment can be derived by evaluating the  $v$  dependence of the determined spectroscopic parameters. For a given bending state-specific parameter,  $a_v$ , an empirical  $v$ -series expansion holds:

$$a_v = a_e + \beta_a(v + 1) + \gamma_a(v + 1)^2 + \dots, \quad (20)$$

where  $a_e$  is the pseudo-equilibrium value of the  $a$  constant purged from the specific  $v$ dependence, while  $\beta_a$  and  $\gamma_a$

represent the expansion coefficients for the first- and second-order contributions, respectively.

From the results presented in Tables 5–7, the quantity  $\beta_a$  can be evaluated for an extensive subset of spectroscopic constants upon excitation of the  $\nu_6$  and  $\nu_7$  quanta, showing that the state-specific parameters we determined for HC<sub>3</sub>N exhibit a remarkable regular behavior. Equation (20) applied to the most important spectroscopic parameters ( $B_v$ ,  $D_v$ , and  $q_v$ ), shows a rapid convergence with only minor departures from the linear trend: 0.5% for the rotational constant, ( $B_v$ ), 3% for the  $q_7$   $l$ -type doubling constant, and 5% and 10% for the quartic ( $D_v$ ) and sextic ( $H_v$ ) centrifugal distortion constants, respectively. Even trends are also shown by the anharmonicity constants  $x_{L(77)}$ ,  $x_{L(67)}$ , and by the  $r_{67}$  vibrational  $l$ -type doubling parameter, whose converged values mildly decrease (1%–2%) upon  $\nu_7$  excitation. Furthermore, no obvious anomalies are exhibited by the high-order coefficients: maximum variations of  $\sim 6\%$  are observed for  $q_{7J}$ ,  $\sim 10\%$  for  $q_{7JJ}$  and  $d_{JL(77)}$ ,  $\sim 30\%$  for  $u_{77}$  and  $r_{67J}$ , and  $\sim 50\%$  for  $u_{77}$  and  $r_{67JJ}$ . These findings are very much comparable with the results of earlier global ro-vibrational analyses performed on related molecules (e.g., Fayt et al. 2004a) and provide a strong indication that the effective Hamiltonian adopted for HC<sub>3</sub>N is adequate for the span and precision of the available data set.

### 6.2. Spectral Predictions

With the spectroscopic constants presented in Tables 5–8, we computed an extensive set of accurate ro-vibrational rest frequencies for all of the vibrational levels of HC<sub>3</sub>N below  $1000 \text{ cm}^{-1}$ . These spectral predictions are provided as digital supporting data and consist of a compilation of IR wavenumbers for all bands observed in this work (see Table 2), plus pure rotational frequencies for all the states listed in Table 3, including interstate transitions. The  $J$  interval selected for the calculation is 0–120. The quadrupole coupling due to the  $^{14}\text{N}$  nucleus was not considered, and thus the computed frequencies for the  $J = 0$ –4 pure rotational transitions correspond to the hypothetical hyperfine-free, unsplit line positions. The estimated uncertainty at the  $1\sigma$  level of each transition frequency is determined statistically by the least-squares fits (Albritton et al. 1976). The data list will also be made available in the Cologne Database for Molecular Spectroscopy (Endres et al. 2016). An excerpt of the data listing is presented in Table 9 for guidance; the following columns are included:

- (1)–(5)  $J'$ ,  $l'_5$ ,  $l'_6$ ,  $l'_7$ ,  $k'$ . Rotational, vibrational angular quantum numbers, and  $e/f$  parity of the upper level.
- (6)–(10)  $J$ ,  $l_5$ ,  $l_6$ ,  $l_7$ ,  $k$ . Rotational, vibrational angular quantum numbers, and  $e/f$  parity of the lower level.
- (11)  $\nu_{J'J}$ . Predicted line position computed from the spectroscopic constants of Tables 5–8.
- (12)  $1\sigma$ . Estimated error of the prediction at the  $1\sigma$  level.
- (13) Units of MHz or  $\text{cm}^{-1}$ . Applies to columns (11) and (12).
- (14)  $S_{J'J}$ . Hönl–London factor.
- (15)  $E_u/k$ . Upper-state energy in K.
- (16)  $g_u$ . Upper-state degeneracy.

The corresponding Einstein A-coefficients for spontaneous emission can then be calculated for each  $J' \rightarrow J$  line using

**Table 9**  
Computed Rest Frequencies for HC<sub>3</sub>N

$J'$	$l'_5$	$l'_6$	$l'_7$	$k'$	$\leftarrow$	$J$	$l_5$	$l_6$	$l_7$	$k$	$\nu_{J'J}$	$1\sigma$	Units	$S_{J'J}$	$E_u/k$	$g_u$
...																
$v_5 = v_7 = 1$																
9	1	0	-1	0 <sup>e</sup>		8	1	0	-1	0 <sup>e</sup>	82159.6651	0.0016	MHz	8.35	1295.3	19
9	1	0	1	2 <sup>e</sup>		8	1	0	1	2 <sup>e</sup>	82168.7926	0.0010	MHz	8.48	1294.7	19
9	1	0	-1	0 <sup>f</sup>		8	1	0	-1	0 <sup>f</sup>	82170.2499	0.0014	MHz	9.00	1293.4	19
9	1	0	1	2 <sup>f</sup>		8	1	0	1	2 <sup>f</sup>	82173.6651	0.0010	MHz	8.48	1294.7	19
...																
$\nu_6$																
18	0	1	0	1 <sup>e</sup>		19	0	0	0	0 <sup>e</sup>	493.12092	0.00003	cm <sup>-1</sup>	4.50	792.4	37
17	0	1	0	1 <sup>e</sup>		18	0	0	0	0 <sup>e</sup>	493.41536	0.00003	cm <sup>-1</sup>	4.25	784.6	35
16	0	1	0	1 <sup>e</sup>		17	0	0	0	0 <sup>e</sup>	493.71032	0.00003	cm <sup>-1</sup>	4.00	777.1	33
15	0	1	0	1 <sup>e</sup>		16	0	0	0	0 <sup>e</sup>	494.00578	0.00003	cm <sup>-1</sup>	3.75	770.1	31
14	0	1	0	1 <sup>e</sup>		15	0	0	0	0 <sup>e</sup>	494.30174	0.00003	cm <sup>-1</sup>	3.50	763.6	29
13	0	1	0	1 <sup>e</sup>		14	0	0	0	0 <sup>e</sup>	494.59820	0.00003	cm <sup>-1</sup>	3.25	757.5	27
...																

**Note.** See column explanations in the text, Section 6.2.

(This table is available in its entirety in machine-readable form.)

(Šimečková et al. 2006)

$$A_{J'J} = \frac{16\pi^3}{3\epsilon_0 h c^3} \frac{\nu_{J'J}^3}{g_u} S_{J'J} \mathfrak{R}^2, \quad (21)$$

where  $\nu_{J'J}$  is the transition frequency,  $S_{J'J}$  is the computed rotational line strength factor (Hönl–London factor) as given in Table 9,  $g_u$  is the upper-level degeneracy (also given in Table 9), and  $\mathfrak{R}^2$  is the squared transition dipole moment (units of C<sup>2</sup> m<sup>2</sup>). For a pure rotational transition,  $\mathfrak{R}^2 = \mu^2$ , where  $\mu$  is the permanent electric dipole moment. For a vibration–rotation transition, the squared transition dipole moment is

$$\mathfrak{R}^2 = |R_{v'v}^0|^2 F, \quad (22)$$

where  $|R_{v'v}^0|$  is the rotationless vibrational transition dipole moment including the appropriate vibrational factors for the hot bands (Fayt et al. 2004b) and  $F$  is the Herman–Wallis factor (Herman & Wallis 1955), which, for linear molecules, is defined as

$$F_{RP} = [1 + A_1 m + A_2^{RP} m^2]^2 \quad \text{for } P \text{ and } R \text{ branch lines,}$$

$$F_Q = [1 + A_2^Q J(J+1)]^2 \quad \text{for } Q \text{ branch lines,}$$

where  $m = -J$  and  $m = J+1$  for the  $P$  and  $R$  branches, respectively. The  $A_n^{PQR}$  coefficients depend on the quadratic and cubic potential constants and express the small effects due to the molecular non-rigidity on the intensity factors (Watson 1987). For regular, semi-rigid molecules, the contribution of the Herman–Wallis factor to  $\mathfrak{R}$  is of only a few percent for high- $J$  values (see, e.g., El Hachtouki & Vander Auwera 2002). However, they should be considered when high accuracy in the relative intensity calculation is required.

### 6.3. Astrophysical Implications

The improved set of molecular data presented here provides a useful guidance for the searches of HC<sub>3</sub>N in extraterrestrial environments and may help to retrieve accurate quantitative information from the observations. We obtained an improved description of the ro-vibrational energies that includes a careful

modeling of various local spectral perturbations. This achievement is beneficial to the IR studies of planetary atmospheres (e.g., Titan), whose outcome relies on the ability to predict accurately the intensity distribution in the hot bands (e.g., Jolly et al. 2007, 2010). More importantly, it helps in interpreting the crowded mm spectra observed toward some chemically rich regions of the ISM.

Belloche et al. (2016) recently published a complete 3 mm spectral survey of the hot molecular core Sgr B2(N2) performed with the Atacama Large Millimeter/submillimeter Array (ALMA). This survey, called “Exploring Molecular Complexity with ALMA” (EMoCA), resulted in the detection of a number of complex organic molecules, including HC<sub>3</sub>N in the ground as well as in many vibrationally excited states (see their Table 4). The LTE modeling of the full HC<sub>3</sub>N spectral profile proved to be successful, with some inconsistencies at 92.1 and 100.4 GHz due to the incorrect predictions for the pair of interacting states  $v_5 = v_7 = 1$  and  $v_4 = 7$ . In fact, these frequencies correspond to  $J = 9, 10$  lines where the crossing between the 0<sup>f</sup> and 2<sup>f</sup> sublevels of the above-mentioned states occurs, hence the corresponding transitions are considerably displaced from their hypothetically unperturbed positions.

Here, we use our new spectroscopic predictions to revisit the analysis of the HC<sub>3</sub>N emission in the EMoCA spectrum of Sgr B2(N2). We model the emission of the vibrationally excited states of HC<sub>3</sub>N above  $v_7 = 1$  assuming local thermodynamic equilibrium (LTE), with the same parameters as derived in Belloche et al. (2016): a source size of 0.9'', a rotational temperature of 200 K, a line width of 5.8 km s<sup>-1</sup>, a velocity offset of -1.0 km s<sup>-1</sup> with respect to the assumed systemic velocity of Sgr B2(N2) of 74 km s<sup>-1</sup>, and a column density of  $5.2 \times 10^{17}$  cm<sup>-2</sup> (see Section. 5.3 of Belloche et al. 2016). The computation was performed using the software WEEDS (Maret et al. 2011), taking into consideration the spectral-window- and measurement-set-dependent angular resolution of the observations. Einstein’s  $A$  constant for each transition was computed using the experimental values of the dipole moment derived by DeLeon & Muentner (1985). The resulting synthetic spectra for the states above 800 cm<sup>-1</sup>,  $v_4 = 1$ ,  $v_7 = 4$ ,  $v_5 = v_7 = 1$ , ( $v_6 = 1$ ,  $v_7 = 2$ ), and  $v_6 = 2$  are

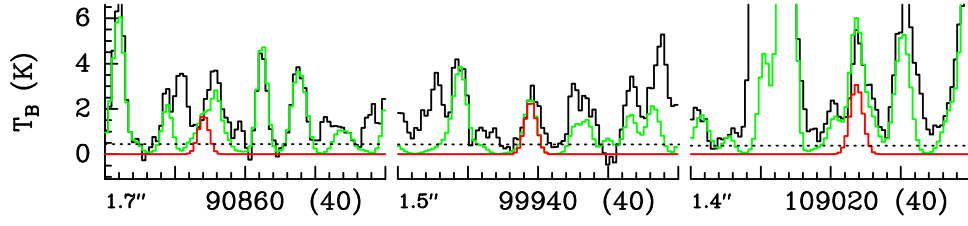


**Figure 8.** Transitions of  $\text{HC}_3\text{N}$ ,  $v_4 = 1$  covered by the EMOCA survey. The best-fit LTE synthetic spectrum of  $\text{HC}_3\text{N}$ ,  $v_4 = 1$  is displayed in red and overlaid on the observed spectrum of Sgr B2(N2), shown in black. The green synthetic spectrum contains the contributions of all molecules identified in the survey so far, including the species shown in red. The central frequency and width are indicated in MHz below each panel. The angular resolution (HPBW) is also indicated. The y-axis is labeled in brightness temperature units (K). The dotted line indicates the  $3\sigma$  noise level.

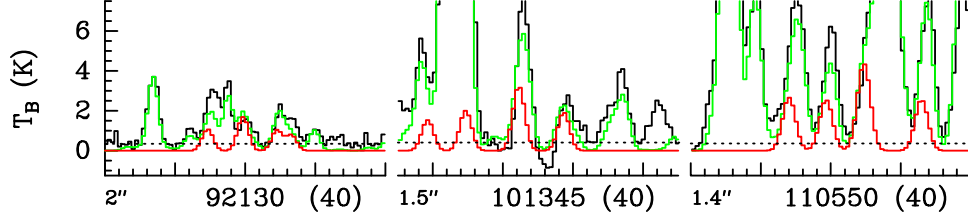


**Figure 9.** Same as Figure 8 for  $v_7 = 4$ .

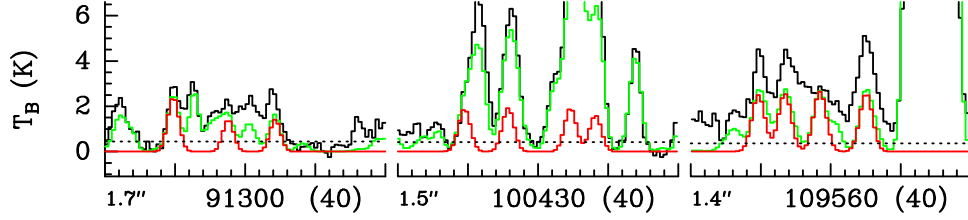


**Figure 10.** Same as Figure 8 for  $v_5 = v_7 = 1$ .

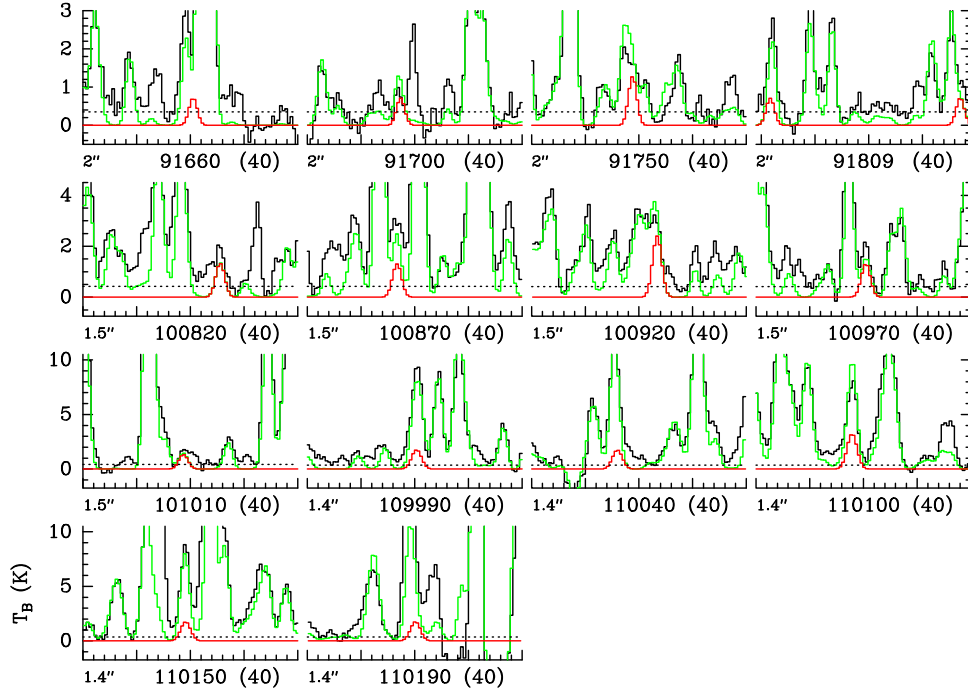


**Figure 11.** Same as Figure 8 for  $v_6 = 1$ ,  $v_7 = 2$ .

overlaid on the ALMA spectrum of Sgr B2(N2) in Figures 8–12.

The model that uses our new spectroscopic predictions gives the same results as the older one for  $v_4 = 1$  and  $v_6 = 2$ , but it

improves the agreement between the synthetic and observed spectra for  $v_7 = 4$  and  $v_5 = v_7 = 1$ , thanks to the proper treatment of the interaction between states in the spectroscopic analysis. This is illustrated in Figures 13 and 14, which display

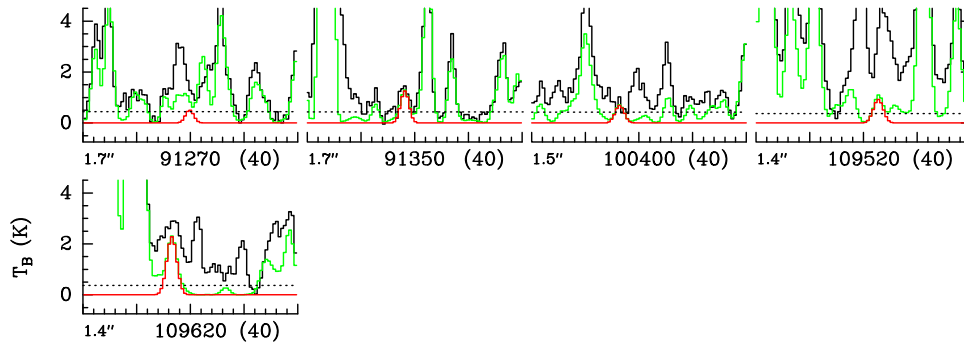
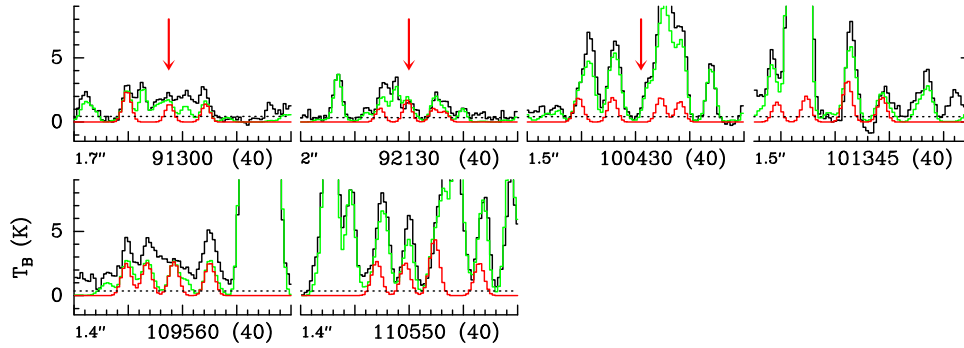
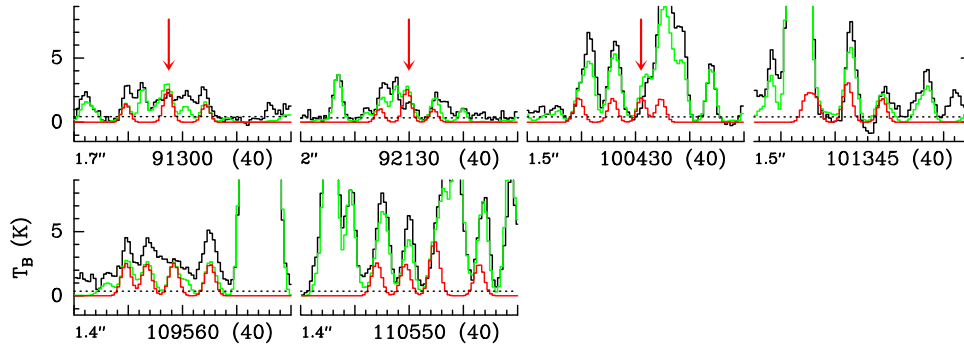
Figure 12. Same as Figure 8 for  $v_6 = 2$ .Figure 13. Same as Figure 8 for  $v_7 = 4$  and  $v_5 = v_7 = 1$  together in order to compare to the older predictions shown in Figure 14. The arrows mark the frequencies where the new spectroscopic predictions improve the agreement between the synthetic and observed spectra.

Figure 14. Same as Figure 13 but using the older spectroscopic predictions as in Belloche et al. (2016). The arrows mark the frequencies where discrepancies between the synthetic and observed spectra are present.

synthetic models computed with the new and old spectroscopic predictions, respectively, over the frequency ranges where  $v_7 = 4$  and  $v_5 = v_7 = 1$  have rotational transitions. In these figures, the arrows indicate the frequencies where the new predictions (Figure 13) solve inconsistencies that were present when using the older ones (Figure 14).

We also show in Figure 11 the synthetic rotational spectrum of the excited state  $v_6 = 1, v_7 = 2$ . Most of its transitions are unfortunately blended with transitions of other species in the ALMA spectrum of Sgr B2(N2). There are, however, two transitions that suffer less from contamination and can be considered as detected (at 100826 and 100970 MHz). Small discrepancies can be seen around 91697 and 100923 MHz, where the model containing all of the identified molecules slightly overestimates the observed spectrum, but these discrepancies are at the  $2\sigma$  level only, and we consider them insignificant. A discrepancy at the  $3\sigma$  level is present around 91748 MHz. The identified emission is dominated by acetone in its  $v_{12} = 1$  state, which is also responsible for the

discrepancy present at 91755 MHz. Therefore, we believe the discrepancy at 91748 MHz is due to an inaccurate modeling of the acetone spectrum and not to  $\text{HC}_3\text{N } v_6 = 1, v_7 = 2$ . Finally, a discrepancy at the  $10\sigma$  level is present around 110098 MHz. Here again, the emission is dominated by acetone in its  $v_{12} = 1$  state, so we suspect that the discrepancy is due to an issue with our LTE model of acetone or with the spectroscopic predictions of this species. Therefore, all in all, we are confident that the  $\text{HC}_3\text{N } v_6 = 1, v_7 = 2$  features are present at the level indicated by our synthetic spectrum. The detection of this excited state was not reported in Belloche et al. (2016) due to the lack of spectroscopic predictions at the time their study was published.

## 7. Conclusion

Cyanoacetylene is a molecule of remarkable astronomical importance and has been observed in a number of sources, both Galactic and extragalactic. These detections relied on laboratory investigations which, however extended, lacked some



essential information concerning the rotational and ro-vibrational spectra. Indeed, knowledge of the fundamentals and of the weak hot bands involved in the IR spectrum, which are necessary to model the molecular profile of planetary atmospheres, was incomplete. Moreover, the pure rotational spectrum of HC<sub>3</sub>N observed in space sometimes could not be assigned successfully because of the density of lines or the incorrect predictions based on laboratory analyses.

This work aims at filling in these gaps by undertaking a full re-investigation of the IR spectrum of HC<sub>3</sub>N up to 1100 cm<sup>-1</sup> by high-resolution FTIR spectroscopy. In addition, several pure rotational transitions in the ground and vibrationally excited states were recorded in the mm and sub-mm regions. In total, all of the transitions present in the literature and newly recorded in this work, involving energy levels below 1000 cm<sup>-1</sup>, form a data set of about 3400 ro-vibrational lines across 13 bands and 1500 pure rotational lines belonging to 12 vibrational states. They were fitted together to an effective Hamiltonian, allowing the determination of 121 spectroscopic constants. Such a global data analysis could not be accomplished without considering explicitly the complex network of vibrationally interacting states.

In the energy interval considered at present are two major resonance schemes: (i)  $v_5 = 1 \sim v_7 = 3$  and (ii)  $v_4 = 1 \sim v_5 = v_7 = 1 \sim v_6 = 2 \sim v_7 = 4$ . The interaction terms of the Hamiltonian are purely vibrational ( $\tilde{H}_{30}$ ,  $\tilde{H}_{40}$ ,  $\tilde{H}_{50}$ ) and ro-vibrational ( $\tilde{H}_{32}$ ,  $\tilde{H}_{42}$ ,  $\tilde{H}_{52}$ ). The isolated states are the ground state,  $v_6 = 1$ ,  $v_7 = 1$ ,  $v_7 = 2$ ,  $v_6 = v_7 = 1$ , and  $v_6 = 1$ ,  $v_7 = 2$ . The energy cutoff of 1000 cm<sup>-1</sup> was chosen so that a complete analysis of the low-lying vibrational states involved in the anharmonic resonances could be performed. Transitions involving higher-energy levels, although detected in our experiments, were not considered in the present study. Some of these higher-level transitions are part of the same interactions but are simply scaled up by one vibrational quanta of  $v_7$ . Rotational, vibrational, and resonance constants were determined from the global fit without any assumption deduced from theoretical calculations or through comparisons to similar molecules. The overall quality of the fit is very satisfactory, and the parameters were derived with very good precision and accuracy. Eventually, it was possible to compute a large set of reliable accurate ro-vibrational rest frequencies for all of the vibrational levels of HC<sub>3</sub>N below 1000 cm<sup>-1</sup> and for pure rotational transitions in the  $J$  range between 0 and 120. This is particularly important for the spectral regions not explored in the laboratory. Our predictions, which form the most accurate and complete set of rest frequencies available for HC<sub>3</sub>N, are especially useful for astronomical searches.

These improved spectral predictions enabled refined analyses of molecular emission observed toward Sgr B2(N2) with ALMA (the EMOCA survey). Discrepancies between observations and the global model (Belloche et al. 2016), produced by perturbed HC<sub>3</sub>N ro-vibrational lines, could be effectively removed. Furthermore, one previously unreported vibrational state of HC<sub>3</sub>N ( $v_6 = 1$ ,  $v_7 = 2$ ) was newly identified in the EMOCA observed spectra.

The authors acknowledge the financial support of the Ministero dell'Istruzione, dell'Università e della Ricerca (PRIN 2012 funds, project STAR; grant number 20129ZFHE) and the University of Bologna (RFO funds). H.S. thanks André Fayt for the initial predictions, which were beneficial for the

study of higher-lying vibrational states of HC<sub>3</sub>N. This paper makes use of the following ALMA data: ADS/JAO.ALMA#2011.0.00017.S, ADS/JAO.ALMA#2012.1.00012.S. ALMA is a partnership of ESO (representing its member states), NSF (USA), and NINS (Japan), together with NRC (Canada), NSC and ASIAA (Taiwan), and KASI (Republic of Korea), in cooperation with the Republic of Chile. The Joint ALMA Observatory is operated by ESO, AUI/NRAO, and NAOJ. The interferometric data are available in the ALMA archive at <https://almascience.eso.org/alma-data/archive>. The work in Cologne and Bonn has been in part supported by the Deutsche Forschungsgemeinschaft (DFG) through the collaborative research grant SFB-956 "Conditions and Impact of Star Formation," project area B3. Part of the early laboratory studies in Cologne were supported through SFB-494.

## ORCID iDs

Luca Bizzocchi  <https://orcid.org/0000-0002-9953-8593>  
 Filippo Tamassia  <https://orcid.org/0000-0003-4145-7827>  
 Jacob Laas  <https://orcid.org/0000-0001-6876-6940>  
 Luca Dore  <https://orcid.org/0000-0002-1009-7286>  
 Paola Caselli  <https://orcid.org/0000-0003-1481-7911>  
 Karl M. Menten  <https://orcid.org/0000-0001-6459-0669>

## References

- Aalto, S., Garcia-Burillo, S., Muller, S., et al. 2012, *A&A*, **537**, A44  
 Albritton, D. L., Schmeltekopf, A. L., & Zare, R. N. 1976, in *Molecular Spectroscopy: Modern Research II*, Vol. 2 ed. K. N. Rao (New York: Academic), **1**  
 Aliev, M. R., & Watson, J. K. G. 1985, in *Molecular Spectroscopy: Modern Research*, Vol. III ed. K. N. Rao (New York: Academic), **1**  
 Arie, E., Dang Nhu, M., Arcas, P., et al. 1990, *JMoSp*, **143**, 318  
 Bell, M. B., Feldman, P. A., Travers, M. J., et al. 1997, *ApJL*, **483**, L61  
 Belloche, A., Müller, H. S. P., Garrod, R. T., & Menten, K. M. 2016, *A&A*, **587**, A91  
 Bizzocchi, L., Dore, L., Degli Esposti, C., & Tamassia, F. 2016, *ApJL*, **820**, L26  
 Bizzocchi, L., Lattanzi, V., Laas, J., et al. 2017, *A&A*, **602**, A34  
 Bizzocchi, L., Tamassia, F., Degli Esposti, C., et al. 2011, *MolPh*, **109**, 2181  
 Brown, J. M., Hougen, J. T., Huber, K.-P., et al. 1975, *JMoSp*, **55**, 500  
 Chapillon, E., Dutrey, A., Guilloteau, S., et al. 2012, *ApJ*, **756**, 58  
 Chen, W., Bocquet, R., Wlodarczak, G., & Boucher, D. 1991, *IIMW*, **12**, 981  
 Cordiner, M. A., Nixon, C. A., Teanby, N. A., et al. 2014, *ApJL*, **795**, L30  
 Costagliola, F., & Aalto, S. 2010, *A&A*, **515**, A71  
 Costagliola, F., Sakamoto, K., Muller, S., et al. 2015, *A&A*, **582**, A91  
 Coustenis, A., Achterberg, R. K., Conrath, B. J., et al. 2007, *Icar*, **189**, 35  
 Creswell, R. A., Winnewisser, G., & Gerry, M. C. L. 1977, *JMoSp*, **65**, 420  
 de Zafra, R. L. 1971, *ApJ*, **170**, 165  
 Decin, L., Agúndez, M., Barlow, M. J., et al. 2010, *Natur*, **467**, 64  
 Degli Esposti, C., Bizzocchi, L., Botschwina, P., et al. 2005, *JMoSp*, **230**, 185  
 DeLeon, R. L., & Muentner, J. S. 1985, *JChPh*, **82**, 1702  
 Dore, L. 2003, *JMoSp*, **221**, 93  
 El Hachetouki, R., & Vander Auwera, J. 2002, *JMoSp*, **216**, 355  
 Endres, C. P., Schlemmer, S., Schilke, P., Stutzki, J., & Müller, H. S. P. 2016, *JMoSp*, **327**, 95  
 Fayt, A., Vigouroux, C., Willaert, F., et al. 2004a, *JMoSt*, **695**, 295  
 Fayt, A., Vigouroux, C., & Winther, F. 2004b, *JMoSp*, **224**, 114  
 Fayt, A., Willaert, F., Demaison, J., et al. 2008, *CP*, **346**, 115  
 Hassel, G. E., Herbst, E., & Garrod, R. T. 2008, *ApJ*, **681**, 1385  
 Herman, R., & Wallis, R. F. 1955, *JChPh*, **23**, 627  
 Horneman, V.-M. 2007, *JMoSp*, **241**, 45  
 Jaber Al-Edhari, A., Ceccarelli, C., Kahane, C., et al. 2017, *A&A*, **597**, A40  
 Jiang, X.-J., Wang, J.-Z., Gao, Y., & Gu, Q.-S. 2017, *A&A*, **600**, A15  
 Jolly, A., Benilan, Y., & Fayt, A. 2007, *JMoSp*, **242**, 46  
 Jolly, A., Fayt, A., Benilan, Y., et al. 2010, *ApJ*, **714**, 852  
 Khelifi, M., Raulin, F., Arie, E., & Graner, G. 1990, *JMoSt*, **143**, 209  
 Khelifi, M., Raulin, F., & Dang-Nhu, M. 1992, *JMoSp*, **155**, 77  
 Lafferty, W. J. 1968, *JMoSp*, **25**, 359  
 Li, J., Wang, J., Gu, Q., Zhang, Z.-y., & Zheng, X. 2012, *ApJ*, **745**, 47

- Lindberg, J. E., Aalto, S., Costagliola, F., et al. 2011, *A&A*, **527**, A150
- Loison, J.-C., Wakelam, V., Hickson, K. M., Bergeat, A., & Mereau, R. 2014, *MNRAS*, **437**, 930
- Loomis, R. A., Shingledecker, C. N., Langston, G., et al. 2016, *MNRAS*, **463**, 4175
- Mallinson, P. D., & de Zafra, R. L. 1978, *MolPh*, **36**, 827
- Maret, S., Hily-Blant, P., Pety, J., Bardeau, S., & Reynier, E. 2011, *A&A*, **526**, A47
- Marten, A., Hidayat, T., Biraud, Y., & Moreno, R. 2002, *Icar*, **158**, 532
- Martín, S., Kohno, K., Izumi, T., et al. 2015, *A&A*, **573**, A116
- Mauersberger, R., Henkel, C., & Sage, L. J. 1990, *A&A*, **236**, 63
- Mbosei, L., Fayt, A., Dréan, P., & Cosléou, J. 2000, *JMoSt*, **517**, 271
- Miller, A. F., & Lemmon, D. H. 1967, *AcSpA*, **23**, 1415
- Moravec, A. 1994, PhD thesis, Köln, University of Cologne
- Mumma, M. J., & Charnley, S. B. 2011, *ARA&A*, **49**, 471
- Nielsen, H. H. 1951, *RvMP*, **23**, 90
- Öberg, K. I., Guzmán, V. V., Furuya, K., et al. 2015, *Natur*, **520**, 198
- Öberg, K. I., Lauck, T., & Graninger, D. 2014, *ApJ*, **788**, 68
- Oka, T. 1967, *JChPh*, **47**, 5410
- Okabayashi, T., Tanaka, K., & Tanaka, T. 1999, *JMoSp*, **195**, 22
- Pardo, J. R., Cernicharo, J., Goicoechea, J. R., & Phillips, T. G. 2004, *ApJ*, **615**, 495
- Peng, Y., Qin, S.-L., Schilke, P., et al. 2017, *ApJ*, **837**, 49
- Pickett, H. M. 1991, *JMoSp*, **148**, 371
- Sakai, N., Sakai, T., Hirota, T., & Yamamoto, S. 2008, *ApJ*, **672**, 371
- Sakai, N., & Yamamoto, S. 2013, *ChRv*, **113**, 8981
- Sanchez, R. A., Ferris, J. P., & Orgel, L. E. 1966, *Sci*, **154**, 784
- Šimečková, M., Jacquemart, D., Rothman, L. S., Gamache, R. R., & Goldman, A. 2006, *JQSRT*, **98**, 130
- Spahn, H., Müller, H. S. P., Giesen, T. F., et al. 2008, *CP*, **346**, 132
- Suzuki, H., Yamamoto, S., Ohishi, M., et al. 1992, *ApJ*, **392**, 551
- Thorwirth, S., Müller, H. S. P., & Winnewisser, G. 2000, *JMoSp*, **204**, 133
- Toth, R. A. 1991, *JOSAB*, **8**, 2236
- Turner, B. E. 1971, *ApJL*, **163**, L35
- Tyler, J. K., & Sheridan, J. 1963, *Trans Faraday Soc*, **59**, 2661
- Uyemura, M., Deguchi, S., Nakada, Y., & Onaka, T. 1982, *Bull. Chem. Soc. Japan*, **55**, 384
- Uyemura, M., & Maeda, S. 1974, *Bull. Chem. Soc. Japan*, **47**, 2930
- Vigouroux, C., Fayt, A., Guarnieri, A., et al. 2000, *JMoSp*, **202**, 1
- Wagner, G., Winnewisser, B. P., Winnewisser, M., & Sarka, K. 1993, *JMoSp*, **162**, 82
- Watson, J. K. G. 1987, *JMoSp*, **125**, 428
- Willacy, K., Allen, M., & Yung, Y. 2016, *ApJ*, **829**, 79
- Winnewisser, G. 1995, *Vib. Spectrosc.*, **8**, 241
- Winnewisser, G., Belov, S. P., Klaus, T., & Schieder, R. 1997, *JMoSp*, **184**, 468
- Wyrowski, F., Schilke, P., Thorwirth, S., Menten, K. M., & Winnewisser, G. 2003, *ApJ*, **586**, 344
- Yamada, K., Schieder, R., Winnewisser, G., & Mantz, A. W. 1980, *ZNatA*, **35a**, 690
- Yamada, K., & Winnewisser, G. 1981, *ZNatA*, **36a**, 23
- Yamada, K. M. T., Birss, F. W., & Aliev, M. R. 1985, *JMoSp*, **112**, 347
- Yamada, K. M. T., & Bürger, H. 1986, *ZNatA*, **41a**, 1021
- Yamada, K. M. T., & Creswell, R. A. 1986, *JMoSp*, **116**, 384
- Yamada, K. M. T., Moravec, A., & Winnewisser, G. 1995, *ZNatA*, **50a**, 1179